TanDEM-X: Deriving InSAR Height Changes and Velocity Dynamics of Great Aletsch Glacier

Silvan Leinss, *Senior Member, IEEE*, and Philipp Bernhard, *Student Member, IEEE*

***Abstract*—Great Aletsch Glacier (Grosser Aletschgletscher), the largest glacier in the European Alps, contains 20% of the entire Swiss ice mass. Therefore, it has been selected as a super-testsite for the TanDEM-X satellite mission. Dense time series with a repeat interval down to 11 d were acquired between 2011 and 2019 using two polarizations (HH and VV) and across-track baselines of 0–1 km. To evaluate the use of interferometric single-pass synthetic aperture radar mission for glaciological applications, we implemented a processing pipeline in interactive data language (IDL) and computed 130 digital elevation models (DEMs) from bistatic radar interferograms. We present a method to circumvent a common pitfall during orthorectification of radar DEM differences. Regression analysis of DEM time series shows a height loss of up to 8 m a^{-1} on the tongue and 1.5 m a^{-1} when averaged over the whole glacier area. In spring 2013, we observed X-band penetration depths of 4 ± 2 m in the accumulation area. For strongly crevassed areas, the coherence drops already to 0.5 for across-track baselines $B_\perp > 200$ m. With patch-based incoherent offset tracking, we obtained an almost complete 200 m resolution velocity map. Velocities reach up to 0.8 m d^{-1}, show a seasonal variability of ±0.05 m d^{-1}, and agree within 0.04 m d^{-1} (root mean square error) with field measurements. Copolar phase differences suggest an approximation of snow accumulation. We demonstrate orthorectification of the backscatter intensity using simultaneously acquired TanDEM-X interferograms, which allows for the decoupling of horizontal velocity estimates from phase-center height changes due to penetration and ice melt.**

***Index Terms*—Common-band filter, copolar phase difference (CPD), digital elevation model (DEM), DEM differencing, geocoding, Great Aletsch Glacier, offset tracking, orthorectification, single pass radar interferometry, TanDEM-X, velocity, wave number shift.**

I. Introduction

GREAT Aletsch Glacier (ger. Grosser Aletschgletscher), the largest glacier in Switzerland, is more than 22-km long, covers about 80 km^2, is up to 800-m thick, and its volume of 15 km^3 contains 20% of the entire Swiss ice mass [1], [2]. Similar to almost all glaciers in the European Alps, Great Aletsch Glacier has shown a strong retreat with around 3 km since 1880 and 400 m within the last ten years [3], [4]. The glacier has been monitored by the bistatic synthetic aperture radar (SAR) formation TanDEM-X [5], [6] since April 2011. Together with the Columbia Glacier in Alaska [7], it has been defined as one of the two alpine super-testsites among other testsites related to cryospheric applications. Aletsch Glacier has been imaged from the same orbit by a time series of about 130 bistatic stripmap acquisitions including 11 pursuit-monostatic acquisitions with varying across-track baselines. During the TanDEM-X science phase (2014/2015) [8], the across-track distance between the two satellites was increased from around 10–100 m and bistatic acquisitions with effective perpendicular baselines of $B_\perp = 1\,\mathrm{km}$ were acquired.

The main purpose of the TanDEM-X mission is the generation of a high precision digital elevation model (DEM) covering 97% of all land masses [9]. This TanDEM-X DEM product, with specified accuracy [10], is mosaiced from multiple acquisitions and is available with 12 and 30 m resolution. The advantage of SAR missions is their weather and daylight independent imaging capability which makes such systems particularly suitable for monitoring snow and glaciers. However, the penetration of microwaves into dry snow, scene, and orbit-dependent noise characteristics, limited coverage due to radar shadow and layover in mountainous terrain, the slant radar view geometry, and phase unwrapping problems can make the interpretation of derived DEMs difficult. Therefore, knowledge about these effects is required for a correct interpretation of radar DEMs and the derived height changes. As the way of dealing with these problems depends on area and application, DEMs are not provided on a per-scene basis. Instead, coregistered single look slant range complex pairs (CoSSC, specified according to [11] and [12]) form the basis for interferometric SAR (InSAR) processing and the generation of per-scene DEMs by the user.

The penetration depends on many parameters such as frequency, polarization, incidence angle, and perpendicular baseline, but also on the snow structure and the water content [13]–[17]. To estimate the penetration bias, various methods focus on correlations among penetration, backscatter signal, and interferometric coherence [18], [19] or on multifrequency, multisensor, or multipolarimetric model-based approaches [16], [20], [21]. Regression over multiyear DEM time series can also reduce the penetration bias, as shown in this study.

Apart from a penetration bias, the accuracy of the generated DEMs depends on the bistatic configuration and on surface properties determining the height noise and the level of the interferometric coherence. In general, the height noise decreases for a smaller height-of-ambiguity h_{amb} which, in turn, is inversely proportional to the baseline $B_\perp$. However, for surface structures, where the vertical variability of the topography approaches

Manuscript received September 30, 2020; revised February 23, 2021; accepted April 21, 2021. Date of publication May 6, 2021; date of current version May 26, 2021. *(Corresponding author: Silvan Leinss.)*

Silvan Leinss was with the Institute of Environmental Engineering, ETH Zurich, 8093 Zurich, Switzerland. He is now with the Laboratoire d'Informatique, Systèmes, Traitement de l'Information et de la Connaissance (LISTIC), Université Savoie Mont Blanc, 74940 Annecy, France. (e-mail: silvan.leinss@univ-smb.fr).

Philipp Bernhard is with the Institute of Environmental Engineering, ETH Zurich, 8093 Zurich, Switzerland (e-mail: bernhard@ifu.baug.ethz.ch).

Digital Object Identifier 10.1109/JSTARS.2021.3078084

h_{amb}, e.g., for crevasses, large baselines can lead to significant decorrelation and frequent phase wrapping errors. This can make DEM generation impossible as observed, e.g., for glacier surges [22]. A similar effect is volume decorrelation [13], [23], [24] which occurs over regions with a strong radar penetration and volume scattering, e.g., on ice sheets when the penetration depth approaches h_{amb} [25]. The interferometric coherence is further impacted by the signal-to-noise ratio of the backscatter signal which is why DEM generation over wet snow and over sandy regions is difficult [26], [27].

Many natural and man-made surface properties show a characteristic response of the radar backscatter signal in different polarizations [28], [29]. Therefore, TanDEM-X has polarimetric imaging capabilities using either two or, experimentally, all four polarization channels. Polarimetric applications usually focus on vegetation characterization (e.g., [30]–[32]) utilizing polarization-dependent scattering properties. In contrast, the microstructure of snow causes a characteristic birefringence which results in significant copolar phase difference (CPD) [33], [34]. It is noteworthy that the CPD is not a scattering effect but an effect of signal propagation in a birefringent medium with negligible absorption. Time series of the CPD can be difficult to interpret, but recent work explains well the temporal and stratigraphic variability of the birefringence in the snow pack [35] and, thereby, the temporal evolution of the CPD.

In this study, we did not rely on external software but implemented a complete processing pipeline to calculate DEMs from the TanDEM-X CoSSC products. Our algorithm includes scene-coregistration, topographic phase simulation, phase-to-height conversion, and orthorectification (often called "geocoding" in the radar community), including the transformation of slant height changes measured in radar coordinates to vertical height changes in map coordinates. In addition, we implemented an algorithm for intensity offset tracking [36] which we used to derive glacier surface velocities from the orthorectified TanDEM-X radar images.

The article is structured as follows. First, we describe the dataset and field measurements. Then, two methods sections outline the InSAR DEM generation and offset tracking considering the relevance of InSAR-based orthorectification of the backscatter intensity. The next section describes the analysis of the generated DEMs, the velocity maps, and the copolar data. In Section VI, we first validate the method with field measurements and compare our results to results obtained from the GAMMA software. Then, we evaluate the DEMs in terms of seasonal variability, radar penetration, coherence loss, and orthorectification problems. Finally, we present a velocity map of Aletsch Glacier, discuss seasonal velocity variations with respect to surface height changes, and validate the velocity with field measurements. In addition, we present the sensitivity of the HH and VV polarization to snow conditions. In Section VII, we compare our results to the predicted evolution of Aletsch Glacier [37], [38] and consider the relevance of our results for glaciological applications.

II. Dataset

A. TanDEM-X Data

The data set contains over 130 bistatic, dual-pol TanDEM-X stripmap acquisitions acquired over the Aletsch region of the Swiss Alps (46.50 N, 8.03 E) shown in Fig. 1. All data were acquired from the same orbit (154) in a descending imaging geometry (looking west) with an incidence angle of about 32°. To explore different bistatic configurations, the effective perpendicular baselines $B_\perp$, determining the height sensitivity for across-track interferometry, were generally small (0–200 m) but were increased up to 1040 m during the large baseline acquisition period in spring 2015. In winter 2014/2015, pursuit monostatic acquisitions with 77 km along-track distance were acquired [8]. Due to the very short temporal baseline (10 s), we also generated DEMs from these acquisitions. Baselines and the corresponding ambiguity heights of our dataset are shown in Fig. 2. Two ascending acquisitions from spring 2011 were not considered in this study.

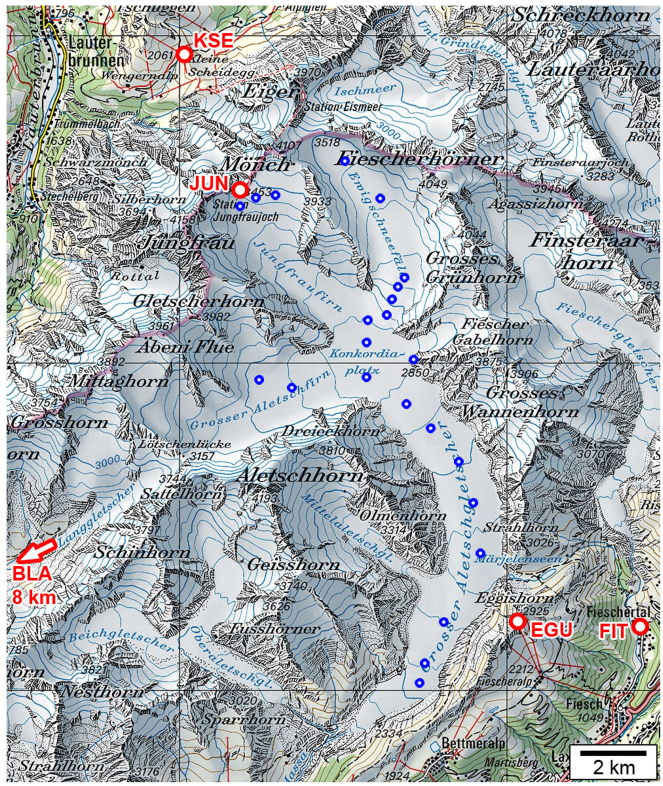

Fig. 1. Map of the study area. Red dots indicate locations of meteorological stations. Blue dots indicate GPS field measurements of the surface velocity and the surface height. Contour intervals are 100 m at orthometric heights (LN02). Areas used for height reference are located in the valleys north and south of the shown area. Source: Federal Office of Topography (SwissTopo).

Almost all data were acquired in the two polarizations HH and VV (two in VV/VH). The spatial resolution in the dual-pol strip map mode was 1.2 × 6.6 m (slant range, azimuth) at a pixel spacing of 1.75 × 2.3 m on the (horizontal) ground.

The orbit repeat interval of TanDEM-X is 11 d. However, due to competing interests, acquisitions could not be acquired in every orbit pass. Therefore, the time series shows gaps of multiples of 11 d. The blue tick marks in Fig. 2 provide an overview of acquisition dates. Because the area is mainly considered as a snow-specific super testsite, most acquisitions are available between October and May with a few acquisitions available in summer 2011 and 2012. Still, snow melt was captured, at least

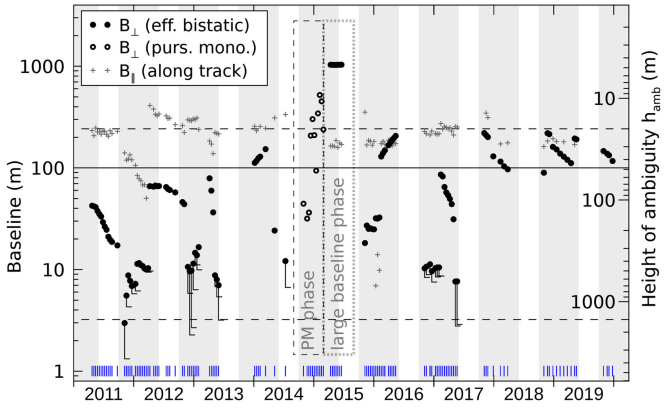

Fig. 2. TanDEM-X effective across-track baselines (dots) and along-track baselines (+) with the corresponding ambiguity heights (right axis) of the dataset containing bistatic (solid dots) and pursuit-monostatic (PM) acquisitions (open circles). Most data were acquired from October to May (gray shading). Summer acquisitions are available in 2011 and 2012. The two horizontal dashed lines indicate an ambiguity height of 20 and 1500 m. The blue ticks visualize the temporal spacing of acquisitions. Whiskers at small baselines indicate the true h_{amb} where $B_\perp$ and h_{amb} deviate from the inverse proportionality used to scale the right axis.

TABLE I
COORDINATES OF WEATHER STATIONS AND AVAILABLE PARAMETERS. P: PRECIPITATION, T: TEMPERATURE

Name,	abbreviation	altitude (m)	lon (deg)	lat (deg)	param.
Kleine Scheidegg	KSE	2061	07°57'34"	46°35'06"	P
Jungfraujoch	JUN	3571	07°59'08"	46°32'51"	T
Blatten	BLA	1538	07°49'24"	46°25'14"	T, P
Eggishorn	EGH	2892	08°05'34"	46°25'36"	T
Fieschertal	FIT	1175	08°08'28"	46°25'40"	P

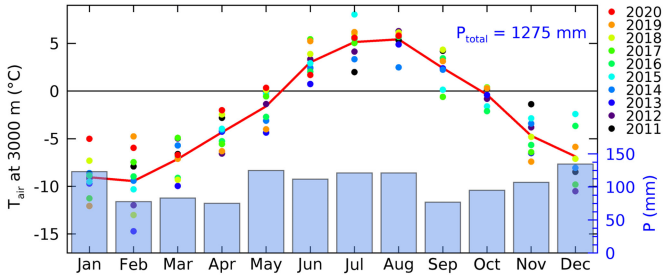

Fig. 3. Monthly mean air temperature calculated for 3000 m from the two meteorological stations at Eggishorn (2892 m a.s.l.) and Jungfraujoch (3571 m a.s.l.). Monthly precipitation is the mean of the three stations BLA, FIT, and KSE listed in Table I. The annual mean precipitation (2011–2019) is 1275 mm.

partially, in eight of nine years in total, including acquisitions from two summer seasons.

B. External DEM and Topography

The alpine topography of the region contains a large elevation range (600–4200 m a.s.l.) with steep slopes at several locations resulting in significant radar layover and shadow which complicated the InSAR processing. The processing was simplified by subtracting a simulated interferogram based on an external DEM before phase unwrapping. For that, we used the high-precision elevation model swissALTI3D provided by the Swiss Federal Office of Topography (SwissTopo). The swissALTI3D is updated at least every six years with data from lidar and optical stereo-correlation. The version we used was generated in 2013 and contains data mainly from 2009. For ice- and snow-free areas, the vertical precision is 0.5 m below 2000 m and 1–3 m above. To speed up the processing, we resampled the horizontal resolution from 2 to 10 m.

C. Field Measurements for Validation

On April 30/May 01, 2019 and 6 d later on May 06/07, 2019, we conducted two field campaigns to measure the surface velocity and surface height at the 22 locations, indicated by blue circles in Fig. 1. For that, we placed 140 cm long bamboo sticks in the snow and measured the position with a geodetic GPS. The accuracy of about 2–3 cm was limited by the diameter of the sticks. Repeated measurements of a reference position showed a GPS accuracy below 1 cm. The reference was located east of Konkordiaplatz on a rock next to the Konkordia hut (P. 2850 in Fig. 1). For each location, we also measured snow depth, limited by the avalanche probe length of 260 cm. To detect manipulation, we placed the sticks in north–south oriented pairs separated by a fixed distance. Coordinates, horizontal displacements, measurement times, and snow depth are listed in Table II.

D. Meteorological Data

For the interpretation of our results, we used data of five different weather stations; names are abbreviated as listed in Table I; red dots in Fig. 1 indicated the location of the stations. The station BLA is located 8 km west of the shown map. From the station data, we generated a climate diagram with monthly mean temperatures and precipitation for the period January 2011 to August 2020 (Fig. 3). The diagram approximates the temperature conditions on Aletsch Glacier at 3000 m by the altitude-weighted mean of the two stations at Jungfraujoch (3571 m) and Eggishorn (2892 m). Mean monthly temperatures rise above 0 °C in late May and drop below zero mid of October. Monthly mean temperatures for each year are plotted as colored dots in Fig. 3.

Precipitation was calculated as the average of the three stations BLA (2638 m), KSE (2061 m), and FIT (1175 m). BLA, west of the study area, and FIT, east of the study area, showed almost equivalent cumulative precipitation despite an altitude difference of about 1 km. In contrast, KSE, situated vertically in between but just north of the main alpine ridge, showed about 50% higher cumulative precipitation. Due to this variability, we did not apply any altitude correction for precipitation. Precipitation gradients in the Alps vary strongly with topography and are difficult to generalize [39]. According to [40], a 50% increase within 1 km height difference is possible. From the three stations, we found that precipitation is relatively homogeneously distributed over the year with an average annual precipitation of 1275 mm (Fig. 3).

III. METHOD I: DEM GENERATION

We developed and implemented algorithms for coregistration, orthorectification, InSAR phase simulation, common band filtering, and DEM generation from TanDEM-X stripmap CoSSC acquisitions and for intensity offset tracking. All code was

TABLE II
NAME, GEOGRAPHIC (GPS) COORDINATES, MEASUREMENT TIMES, AND HORIZONTAL SHIFT (IN SWISS COORDINATES) OF THE *IN SITU* VELOCITY MEASUREMENTS. THE LAST POINT (KK) WAS MEASURED ON THE ROCK NEXT TO THE FLAG OF KONKORDIA HUT. THE ORTHOMETRIC HEIGHT (LN02) OF THIS POINT (2848.60 M) IS 53.30 LOWER THAN THE LISTED ELLIPSOIDAL HEIGHT

Pt	lon (deg)	lat (deg)	Ellips. height (m)	GPS start (first trip)	GPS start (second trip)	shift-E (m)	shift-N (m)	snow depth
P00	7.9840	46.5431	3392.25	2019-04-30 11:29:03	2019-05-06 10:35:37	0.195	-0.522	-
P01	7.9904	46.5455	3495.35	2019-04-30 12:28:52	2019-05-06 11:30:25	-0.266	-0.533	-
P02	7.9979	46.5461	3504.58	2019-04-30 12:59:42	2019-05-06 11:56:35	0.036	-0.577	-
P03	8.0257	46.5554	3466.93	2019-04-30 14:18:52	2019-05-06 13:06:26	0.328	-0.335	-
P04	8.0401	46.5448	3361.51	2019-04-30 14:56:58	2019-05-06 13:28:40	0.502	-0.702	-
P05	8.0498	46.5228	3167.30	2019-04-30 15:32:58	2019-05-06 13:52:20	-0.354	-2.361	-
P06	8.0470	46.5204	3128.02	2019-04-30 15:50:39	2019-05-06 14:07:20	-1.390	-3.096	-
P07	8.0445	46.5173	3049.89	2019-04-30 16:18:38	2019-05-06 14:20:47	-2.837	-3.335	-
P08	8.0421	46.5127	2864.36	2019-04-30 16:40:45	2019-05-06 14:41:33	-1.871	-2.094	-
P09	8.0348	46.5117	2787.53	2019-04-30 16:58:42	2019-05-06 14:58:47	-0.091	-1.132	-
P10	8.0344	46.5054	2744.41	2019-05-01 07:13:49	2019-05-06 15:16:29	0.390	-0.929	-
P11	7.9907	46.4952	2977.16	2019-05-01 08:49:09	2019-05-06 16:41:40	0.499	-0.768	215
P12	8.0044	46.4932	2897.60	2019-05-01 09:08:57	2019-05-06 17:03:25	1.738	0.966	170
P13	8.0338	46.4959	2729.18	2019-05-01 09:32:47	2019-05-06 17:29:05	1.448	-0.205	260
P14	8.0500	46.4882	2639.28	2019-05-01 09:49:55	2019-05-07 05:57:10	1.428	-1.940	250
P15	8.0595	46.4817	2557.53	2019-05-01 10:04:23	2019-05-07 07:42:27	1.447	-1.925	260
P16	8.0704	46.4726	2483.36	2019-05-01 10:20:47	2019-05-07 07:57:44	0.938	-1.494	240
P17	8.0757	46.4612	2431.50	2019-05-01 10:37:34	2019-05-07 08:14:47	0.471	-1.624	210
P18	8.0780	46.4472	2341.22	2019-05-01 10:53:31	2019-05-07 08:33:17	-0.104	-1.661	200
P19	8.0633	46.4284	2141.56	2019-05-01 11:17:44	2019-05-07 09:03:27	-0.960	-1.226	130
P20	8.0562	46.4174	2055.19	2019-05-01 11:37:01	2019-05-07 09:21:00	-0.249	-1.195	80
P21	8.0542	46.4120	1973.13	2019-05-01 11:58:47	2019-05-07 09:38:37	-0.763	-0.787	80
KK	8.0530	46.5006	2901.90	-	2019-05-06 18:32:26	-	-	-

written in IDL. For phase unwrapping, we used the external software SNAPHU [41]. The processing follows ideas by [42] and [43]; details are described in the following sections.

A. Scene Coregistration and Resampling

All single-look complex (SLC) images were coregistered to a common reference scene "ref" (April 06, 2013) with subpixel precision [44] using phase correlation on intensity [45] and patch sizes between 512 and 2048 pixels. The offset field was iteratively approximated by a 2-D linear function and outliers of more than two standard deviations were removed. For resampling, we used a parametric cubic convolution with $\alpha = -0.75$ [46] to approximate a truncated sinc convolution [47].

B. Orthorectification Based on an External DEM

For orthorectification based on an external DEM (cf., InSAR-based orthorectification in Section III-H), we calculated an initial lookup table for the reference image in geographic coordinates by solving the range-Doppler equations given in [48]. The lookup table contains for each point $\vec{P}$ of the external DEM the corresponding azimuth and slant range coordinate. We simplified the range-Doppler equations considering that TanDEM-X stripmap data are zero-Doppler processed ($f_\mathrm{d} = 0\,\mathrm{Hz}$) and that the orbit state vectors $\vec{S}$ are given in the earth-fixed, terrestrial reference frame ITRF2008 where the earth rotation $\omega = 0\,\mathrm{s}^{-1}$. Then, the Doppler equation decouples from the range equation

$$f_d = 0 \stackrel{!}{=} \vec{V}_s \cdot \left(\vec{P} - \vec{S}\right). \tag{1}$$

Solving this equation iteratively in Cartesian Earth centered coordinates for each point $\vec{P}$ provides the azimuth pixel location a_z corresponding to the given orbit state vector $\vec{S}(a_z)$ and velocity $\vec{V}_s(a_z)$. The slant range R follows directly from

$$R = |\vec{P} - \vec{S}|. \tag{2}$$

To transform the orthometric heights of the national leveling network LN02 of the swissALTI3D to ellipsoidal heights (GRS80), we calculated the height difference using the service REFRAME [49] and added it to the orthometric heights of the swissALTI3D. The difference ranges from +46 to +55 m.

C. Calculation of the Simulated Interferometric Phase

To simplify phase unwrapping in any interferometric combination of images i, j selected from a coregistered stack, we calculated for each image the topography-induced propagation phase difference with respect to the reference image "ref"

$$\Delta\varphi_{i,\mathrm{ref}} = \frac{2\pi}{\lambda}\left(r_\mathrm{i} - r_\mathrm{ref}\right). \tag{3}$$

Here, λ is the radar wavelength and r_i, r_ref are the total distances from the transmit antenna (TX) to the ground and back to the receive antenna (RX) of the acquisitions i and "ref." For an interferometric pair i, j of two monostatic images, we can use (2) in (3) to set $r = 2R = 2\overline{SP}$ and to obtain the simulated topographic phase

$$\Delta\varphi_{i,j} = \Delta\varphi_{i,\mathrm{ref}} - \Delta\varphi_{j,\mathrm{ref}} = \frac{4\pi}{\lambda}\left(R_\mathrm{i} - R_\mathrm{j}\right). \tag{4}$$

The phase pattern close to the satellites in Fig. 4 illustrates the spatial distribution of the "phase-rays" described by (4). Extended to the surface, these "phase-rays" can be interpreted as "illuminating" the terrain with the interferometric phase pattern. The true terrain is "sampled" by the range resolution of the radar (indicated by the iso-range arcs in Fig. 4) which results in a measured interferogram in radar coordinates.

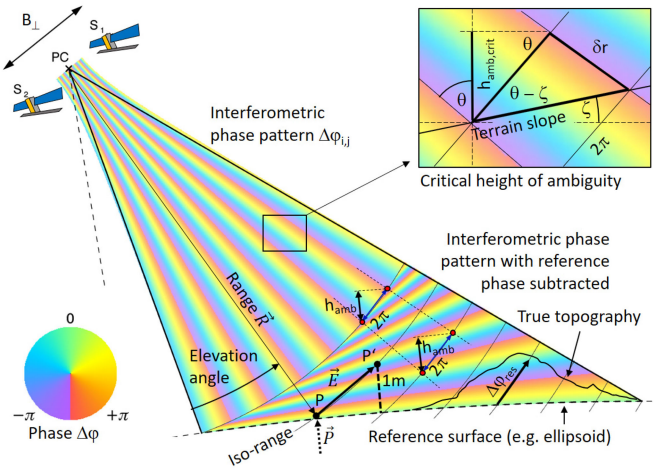

Fig. 4. Visualization of the interferometric phase pattern according to (3) which "illuminates" the terrain (upper left area); the lower right area shows the phase pattern where the simulated topographic phase has already been subtracted. The topographic phase is defined by the illumination phase on the reference surface (here, the ellipsoid) and is constant on iso-range. Therefore, on constant range, the phase pattern changes equally fast independent on whether the reference phase has been subtracted or not. The same holds for h_{amb}. The phase difference along the vector $\vec{E}$ defines the height sensitivity k_z. In the upper right box, a phase wrap occurs within one range resolution cell δr which defines the critical ambiguity height $h_{\text{amb,crit}}$ for terrain of the slope ζ. The radar incidence angle is given by θ.

For the bistatic satellite formation TanDEM-X, consisting of the two satellites TerraSAR-X and TanDEM-X, several transmit/receive modes exist and each satellite can act as transmitter, receiver, or both [6], [50], resulting in either bistatic or monostatic images. Considering the bistatic imaging geometry in (3) gives

$$\Delta\varphi_{i,\text{ref}} = \frac{2\pi}{\lambda}\left(\left(\overline{S_{i,\text{TX}}P} + \overline{PS_{i,\text{RX}}}\right) - \left(\overline{S_{\text{ref,TX}}P} + \overline{PS_{\text{ref,RX}}}\right)\right) \tag{5}$$

with $S_{\cdot,\ldots}$ being the orbit state vectors of the transmitting and receiving satellites. The overline indicates the distance between points. For an interferogram of an arbitrary acquisitions pair $i, j \neq$ "ref," the phase of the reference cancels out when differencing (5) for i, j like in (4).

For a TanDEM-X single-pass interferogram, formed by two images i (monostatic) and i' (bistatic) acquired at the same time, the simulated topographic phase is

$$\Delta\varphi_{i,i'} = \frac{2\pi}{\lambda}\left(\underbrace{\left(\overline{S_{\text{i,TX}}P} + \overline{PS_{\text{i,RX}}}\right)}_{\text{monostatic two-way range}} - \underbrace{\left(\overline{S_{\text{i',TX}}P} + \overline{PS_{\text{i',RX}}}\right)}_{\text{bistatic two-way range}}\right) \tag{6}$$

with collocated $S_{\text{i,TX}} = S_{\text{i,RX}} = S_{\text{i',TX}}$. The computation of (5) can be done in radar coordinates where the elevation model represented by $P(r_g, a_z)$ is obtained by inversion of the geocoding lookup table through triangulation and gridding. To avoid azimuth phase ramps, we shifted the azimuth coordinate of the orbit state vectors of the coregistered scenes by the azimuth shift with respect to the reference scene.

D. Residual Topographic Phase

The difference between the measured interferogram $\Delta\varphi_{i,i,'\text{meas}}$ and the simulated interferometric phase $\Delta\varphi_{i,i'}$ is the residual topographic phase

$$\varphi_{\text{res}} = \Delta\varphi_{i,i,'\text{meas}} - \Delta\varphi_{i,i'}. \tag{7}$$

Even though this might be considered as common knowledge [42], [43], we consider it as important here to visualize the geometry of the residual phase in Cartesian coordinates because ignoring its geometry during orthorectification seems to be a frequent pitfall for InSAR DEM generation.

Fig. 4 illustrates that the residual phase φ_{res} measures the phase angle between the actual topography (solid line) and the reference surface (dashed) *in the direction along iso-range*. The residual phase describes not a vertical height difference. The spatial distribution of φ_{res} in Cartesian coordinates is illustrated by the colored phase pattern that follows approximately the curvature of the reference surface in Fig. 4. By definition of (7) φ_{res} is zero on the reference surface defined by the external DEM. The distribution of φ_{res} in the illustrated geometry is obtained by the difference between the illuminating phase field (the phase rays) and the simulated topographic phase field (not shown). The simulated phase field is constant for iso-range, i.e., orthogonal to the illuminating phase field and is defined by the value of the illuminating phase field on the reference surface.

E. Calculation of the Phase-to-Height Conversion Factor k_z

The factor k_z is used to convert the (residual) topographic phase φ_{res} into a height difference Δh_{res}, which could be added back to the reference surface in order to obtain an elevation model in radar coordinates. However, the commonly given equation of the phase-to-height conversion factor

$$k_z = \frac{4\pi}{\lambda}\frac{B_\perp}{R\sin\theta} \tag{8}$$

is *an approximation* which may deviate by several percent from the true value (in our data about +7% for baselines $B_\perp > 10\,\text{m}$ with larger deviations for smaller baselines).

Using approximation (8) can therefore lead to systematic errors in derived DEMs [a derivation of (8) from (5) can be found, e.g., in [51, Section 1.8]]. Furthermore, confusion may arise about the definition of the effective perpendicular baseline $B_\perp$: for the bistatic mode of TanDEM-X, $B_\perp$ corresponds to the distance between the monostatic and the bistatic phase centers which is about half the perpendicular distance between the orbit state vectors. For monostatic acquisitions, $B_\perp$ corresponds to the full perpendicular distance between the two orbits. Further problems arise because k_z (as well as θ and $B_\perp$) depends on height and range as illustrated by the nonparallel iso-phase planes of ϕ_{res} in Fig. 4. Therefore, k_z needs to be calculated for points as close as possible to the true topography when not replaced by another higher order method or function; see, e.g., [52] and also Section III-H.

To avoid systematic errors from approximation (8), we use (5) to obtain a precise numerical calculation of the phase-to-height conversion factor k_z. For that, we calculate how much the residual phase at a specific radar pixel location (i.e., with fixed range and azimuth) changes when its elevation increases

by a height of 1 m. Under these constrains, we need to shift the point P by the vector $\vec{E}$ as illustrated in Fig. 4. The direction of $\vec{E}$ is determined by the cross section of the iso-range and iso-azimuth planes. The length of the vector $\vec{E}$ must be given such that $\vec{E}$ corresponds to a gain in elevation of 1 m measured *normal* to the earth ellipsoid (Fig. 4). Because the direction of $\vec{E}$ is *not* normal to the earth ellipsoid, the point P' defined by the vector

$$\vec{P}' = \vec{P} + \vec{E} \tag{9}$$

is located at a horizontal location different from the point P. The length of $\vec{E}$ is defined by the scaling factor k_E which can be determined by the condition

$$\vec{E} \cdot \frac{\vec{P}}{|\vec{P}|} \stackrel{!}{=} 1\,\mathrm{m} \quad \text{with} \quad \vec{E} = k_E(\vec{R}_{\mathrm{ref}} \times \vec{V}_{s,\mathrm{ref}}). \tag{10}$$

Recalculating (5) for P' results in the desired relation

$$k_{z,i} = \frac{\text{phase in radian}}{\text{1 m height difference}} = \frac{\Delta\varphi_{i,\mathrm{ref}}(\vec{P}) - \Delta\varphi_{i,\mathrm{ref}}(\vec{P}')}{1\,\mathrm{m}}. \tag{11}$$

This expression is the phase-to-height conversion factor. Similar to (6), the contribution of the reference scene cancels out when calculating $k_{z,i,j} = k_{z,i} - k_{z,j}$ for an interferometric image pair i, j. With that, one can calculate the residual height

$$\Delta h_{\mathrm{res}} = \phi_{\mathrm{res}}/k_z \tag{12}$$

(in radar coordinates) from the residual phase ϕ_{res} obtained by unwrapping φ_{res}, (7). However, when the residual phase does not show any phase wraps, unwrapping is superfluous.

Due to the curvature of the iso-range planes, (9) describes a linear expansion for small height differences close to the reference surface. For large height differences of many hundreds of meters, k_z can be calculated in dependence on, e.g., the residual phase angle.

F. Height of Ambiguity

Equation (11) can be used to determine the height difference h_{amb} which corresponds to a phase difference of 2π. Direct inversion results in the height of ambiguity

$$h_{\mathrm{amb}} = \frac{2\pi}{k_z} \qquad \left(\approx \frac{\lambda R \sin\theta}{2B_\perp}\right). \tag{13}$$

The height of ambiguity is often approximated using (8) as indicated in the parenthesis.

The height of ambiguity remains unaffected when subtracting the topographic phase from the measured interferogram, (7). Fig. 4 illustrates that, independent on whether the topographic phase has been subtracted or not, a phase change of 2π constrained to *iso-range* always corresponds to a height change of h_{amb} normal to the ellipsoid. The reason is that the simulated topographic phase field is constant on iso-range and, therefore, any phase difference measured along iso-range is unaffected by the topographic phase.

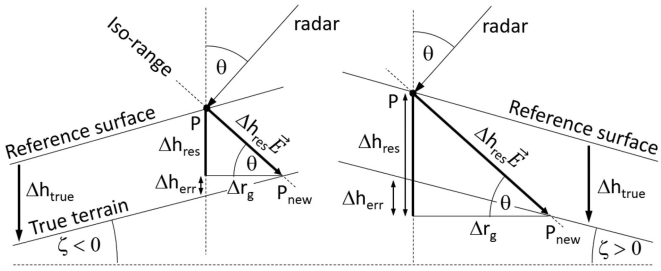

Fig. 5. Illustration of the height change Δh_{true} in map coordinates, the height change Δh_{res} measured in radar coordinates, and the resulting height error $\Delta h_{\mathrm{err}} = \Delta h_{\mathrm{res}} - \Delta h_{\mathrm{true}}$ when the horizontal shift in ground range direction Δr_{g} is not considered. Left image for terrain slope facing away from the radar ($\zeta < 0$) and right image for terrain facing toward the radar (slope $\zeta > 0$).

G. Height Calibration and Correction of Residual Phase Ramps

To correct for possible linear phase ramps in the residual phase ϕ_{res}, we estimated the ramp by a linear fit in all ice-free terrains and subtracted the fitted phase plane from ϕ_{res}. Because the linear fit can be biased by changes in snow height, we applied a vertical calibration of the DEM difference Δh_{res} in radar coordinates. For that, we used nine different locations that were free of snow, ice, and tall vegetation and that were located in the valleys northwest and south of the study area shown in Fig. 1. Then we calibrated Δh_{res} by subtracting the median residual height of these locations.

H. Orthorectification Based on the Estimated InSAR DEM

An apparently frequently used approach to estimate height differences over glaciers is to orthorectify the estimated residual height Δh_{res} derived from the interferogram in slant-range coordinates using the lookup table obtained from an external DEM and then to add the orthorectified height difference back to the external DEM. We like to point out that this approach is only correct for horizontal terrain and only for elevation changes which vary relatively slowly in the horizontal direction. For slopes facing toward or away from the radar, systematic height errors Δh_{err} appear because the SAR interferogram represents height differences Δh_{res} measured along the iso-range direction and not the true height differences Δh_{true} measured in the vertical direction of the map coordinates. Fig. 5 illustrates the problem. To avoid such systematic errors, we generated the final DEM by strict consideration of the slant-range imaging geometry. For that, we added to every point P of the external DEM (in map coordinates) the vector $\vec{E}$, scaled by the calibrated residual phase ϕ_{res} divided by k_z

$$\vec{P}_{\mathrm{new}} = \vec{P} + \vec{E}\frac{\phi_{\mathrm{res}}(\vec{P})}{\Delta\varphi(\vec{P}) - \Delta\varphi(\vec{P}')} = \vec{P} + \Delta h_{\mathrm{res}}\vec{E}. \tag{14}$$

The resulting irregular spaced point cloud $\vec{P}_{\mathrm{new}}$ was then triangulated and gridded to obtain a regular gridded DEM in map coordinates. With this method, we obtained a precise estimation of the topography even when the external DEM deviates significantly from the true topography.

The expected height error $\Delta h_{\text{err}} = \Delta h_{\text{res}} - \Delta h_{\text{true}}$ can be derived from Fig. 5. With $\tan\theta = \Delta h_{\text{res}}/\Delta r_{\text{g}}$ and $\tan\zeta = \Delta h_{\text{err}}/\Delta r_{\text{g}}$, we obtain a relative height error of

$$h_{\text{r,err}} = \frac{\Delta h_{\text{err}}}{\Delta h_{\text{true}}} = \Delta h_{\text{true}} \frac{\tan\zeta}{\tan\theta - \tan\zeta}. \tag{15}$$

I. Loss of Interferometric Coherence

Radar interferometry requires a sufficient similarity of the two radar images from which the interferogram is calculated. The similarity can be estimated using the complex normalized cross-correlation coefficient (the interferometric coherence)

$$\gamma_{i,j} = |\gamma_{i,j}| \exp(\imath \Delta\varphi_{i,j,\text{meas}}) = \frac{\langle A_i A_j^* \rangle}{\sqrt{\langle |A_i|^2 \rangle \langle |A_j|^2 \rangle}} \tag{16}$$

where A_i, A_j are the SLC pixel values of the radar images i and j, $\langle\cdot\rangle$ is a spatial averaging operator, * denotes the complex conjugation, and $\imath = \sqrt{-1}$ is the complex unity. The phase of the coherence $\Delta\varphi_{i,j,\text{meas}}$ corresponds to the measured interferogram.

To avoid coherence loss due to strong phase gradients, we subtracted the simulated interferometric phase, (6), by replacing the nominator $\langle A_i A_j^* \rangle$ in (16) by $\langle A_i e^{-\imath \Delta\varphi_{i,j}} A_j^* \rangle$ so that the coherence returns the residual phase φ_{res}. To reduce phase noise in acquisitions with small baselines, we used a relatively large spatial window of 11×11 px (full width of half maximum of a 2-D Gaussian smoothing kernel) in $\langle\cdot\rangle$.

The coherence can be significantly reduced for terrain which shows a vertical variability close or larger than h_{amb} which was not "flattened" by the simulated topographic phase or for materials where the volume scatters over a similar large height range. Hence, coherence loss can occur already for much smaller baselines than the critical baseline (Section III-J).

The TanDEM-X data over Aletsch Glacier were acquired in two polarizations (HH and VV) because the HH-VV phase difference provides information about the snow structure [33], [35]. However, we expect no significant penetration difference between the two different polarizations. To benefit from both polarizations for DEM generation, the complex coherence was calculated for each polarization separately and was then averaged. Despite the fact that the HH and VV polarization are not completely statistically independent (the magnitude of the HH-VV coherence ranges between 0.5 and 0.7 for snow over soil [34]), averaging helped for phase noise reduction. An analysis of differences between the two polarization is described in Section V-D.

J. Critical Baseline

The effective critical baseline [23], [53], [54] is given by

$$B_{\text{crit}} = \frac{f_{\text{bw}} \lambda R \tan(\theta - \zeta)}{c} \tag{17}$$

where $\zeta > 0$ is the terrain slope facing the radar ($\zeta > 0$ facing off the radar), f_{bw} is the frequency bandwidth of the radar, and c the speed of light. For our bistatic data ($f_{\text{bw}} = 150$ MHz, $\theta = 32.2^\circ$, and $R = 580$ km), the effective critical baseline is $B_{\text{crit}} = 5.7$ km corresponding to a perpendicular distance of $2B_{\text{crit}} = 11.4$ km between the satellites [50].

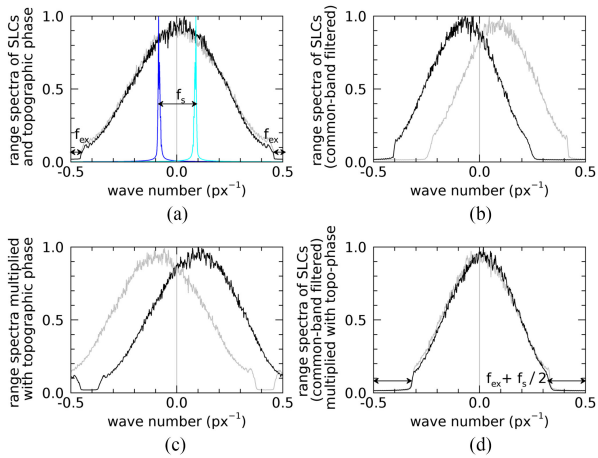

Fig. 6. Illustration of the used method for range common-band filtering. (a) Range spectra of two SLCs (in gray and black) and spectra of two halves of the topographic phase $\pm\frac{1}{2}\Delta\varphi_{\text{ref}}$ (in blue and cyan). (b) After topographic phase removal, the range spectra of the SLCs are misaligned. (c) Range spectra of the common-band filtered SLCs show a reduced bandwidth and are reweighted according to the wave number f_s of the topographic phase. (d) After topographic phase removal, the spectra of the common-band filtered SLCs show an optimal overlap.

At the critical baseline, the interferometric coherence is completely lost because the interferometric phase wraps already within a single slant-range resolution cell of length $\delta r = c/(2f_{\text{bw}})$. This follows directly when inserting (17) into (13) resulting in the "critical height of ambiguity"

$$h_{\text{amb,crit}} = \frac{c}{2f_{\text{bw}}} \frac{\sin\theta}{\tan(\theta - \zeta)} = \delta r \frac{\sin\theta}{\tan(\theta - \zeta)}. \tag{18}$$

As illustrated in the inset of Fig. 4, the terrain of slope ζ captured by the resolution cell of length δr is then illuminated by a radar beam which has the angular width corresponding to an interferometric phase difference of exactly 2π. The elevation gain $h_{\text{amb,crit}}$ along the illumination arc length of $\delta r/\tan(\theta - \zeta)$, which is parallel to $\vec{E}$, follows by multiplication with $\sin\theta$.

K. Range Common-Band Filtering

When subtracting the simulated topographic phase from the large baseline interferograms, as described in Section III-I, a significant wave number shift [55] can occur. The reason is that the large phase gradients of $\Delta\varphi_{i,j}$ misalign the range spectra of each interferometric SLC pair by the corresponding fringe frequency f_s (units: phase cycles per pixel) as illustrated in Fig. 6(a) and (b). The misaligned spectra result in a reduction of the interferometric coherence. To obtain fully overlapping range spectra and to improve the coherence of the large-baseline acquisitions, we implemented a fringe-adaptive range common-band filter [56]–[58] based on patchwise processing of the SLC pairs before coherence calculation. As shown in Fig. 6(d), our common range filter ensures an optimal overlap of range spectra after the phase ramps of the synthetic phase have shifted the SLC spectra. Furthermore, our filter preserves the original shape of the range spectra which avoids sidelobes or blurring of the images.

For implementation, we first estimated the global spectral weighting function from the range spectrum of an SLC pair and also the excess bandwidth f_{ex} originating from the oversampled SLC data [Fig. 6(a)]. To locally estimate the wave number shift, the coregistered image pair was split into overlapping blocks of 100×100 pixels weighted by a Gaussian window to provide smooth transitions between the blocks. For each block pair, the wave number shift f_s was calculated from the fringe frequency of the corresponding simulated phase (optionally also directly from the measured interferogram). After FFT of the blocks, all frequencies are given in wave numbers per pixel (px^{-1}); no information about system frequency or pixel spacing is required. To apply the wave number shift to each block pair, we first flattened the spectrum by removing the global weighting function. Then, we computed identical spectral weights by scaling the bandwidth $b_{\text{w}} = 1 - 2f_{\text{ex}}$ of the global weighting function to the width $b_{\text{w,filtered}} = 1 - f_s - 2f_{\text{ex}}$ of the overlapping spectrum. Then, the new spectral weighting functions were shifted against each other by f_s and were multiplied with the flattened spectrum of the two corresponding blocks. No frequency or phase shifts were applied to the range spectra during filtering as we only reweighted the spectra. During calculation of the residual phase, the multiplication with the simulated topographic phase shifts the filtered spectra such that after filtering, the spectral overlap is optimal and follows the original spectral weighting function (e.g., a hamming window), however, with a reduced bandwidth [Fig. 6(d)].

IV. Method II: Offset Tracking

Our velocity estimation is based on patchwise incoherent offset tracking [36] implemented by cross-correlation of intensity images in dB. To reduce radar speckle, the intensity images were obtained by averaging the backscatter intensity from the four SLC images contained in a dual-pol CoSSC TanDEM-X pair. Offset tracking was performed in map coordinates of 2 m resolution using a patch size of 96×96 pixels (200×200 m). To obtain a denser sampling of the velocity vectors, we used an overlap of 75% resulting in a spatial sampling distance of 32×32 pixels (50 m) of the velocity maps.

The peak position of the 2-D cross-correlation function was determined with subpixel accuracy [44] and converted to velocity. The quality of the cross-correlation function follows from a combination of factors but is mainly determined by the height of the correlation peak above the noise floor. The quality factor q ranges between 0 and 1 and velocity estimates with $q > 0.5$ are usually reliable.

As illustrated in Fig. 2, acquisitions are not equally spaced due to some missing acquisitions. To obtain more complete time series of velocity estimates, we run offset tracking for all pairs with 11, 22, and 33 d time difference and for 44 d where larger gaps exist between the acquisitions. In total, we obtained 89 pairs with $\Delta t = 11$ d, 87 pairs with $\Delta t = 22$ d, 77 pairs with $\Delta t = 33$ d, and 5 pairs with $\Delta t = 44$ d.

A. InSAR-Based Orthorectification of Backscatter Intensity

The seasonal and long-term mass dynamics of glaciers make external DEMs almost always outdated. As a consequence, the DEM heights can deviate many tens of meters from the true topography resulting in horizontal orthorectification shifts of the same order of magnitude as the vertical errors which can strongly affect velocity estimates. To date, TanDEM-X is the only SAR mission which provides a high-resolution DEM and high-resolution radar images for exactly the same acquisition time. Therefore, the satellite formation can provide 3-D backscatter point clouds which can be projected into any desired geometry.

To demonstrate the feasibility of the InSAR-based orthorectification and to analyze the influence on velocity estimates, we generated two different time series of orthorectified backscatter images. For the first series, we used the common way of orthorectification based on the external DEM (swissALTI3D). To avoid distortions due to a strong local micro-topography like crevasses, we applied a Gaussian low-pass filter with a full width of half maximum of 50 m to the orthorectification lookup table. For the second series, we applied an InSAR-based orthorectification of the backscatter intensity using (14) which corresponds to orthorectification using the TanDEM-X DEM generated for the associated acquisition date. In this case, the backscatter signal is orthorectified to the depth of the interferometric phase center which is, by definition, the location where the most backscatter return originates from. With this method, changing penetration depths do not appear as a range-displacement. To reduce distortions due to phase noise of the interferograms as much as possible, we smoothed the residual height Δh_{res} with a 200 m low-pass filter, corresponding to the size of the cross-correlation window.

V. Analysis

A. Validation of Generated DEMs

Because of the significant retreat of Aletsch Glacier, the swissALTI3D, generated from data from around 2009, could not be used for validation of the generated DEMs. Therefore, we used the GPS measurements acquired during the field trip on May 06/07, 2019 and compared the measured heights with the InSAR DEM generated from the acquisition of May 07, 2019 ($h_{\text{amb}} = 25$ m). During the field trip, snow conditions were generally dry with temperatures slightly below zero indicating that penetration into snow can occur. To correct for the penetration bias, we added the snow depth measured in the field to the TanDEM-X heights.

In addition, we compared our results from April 06, 2013 with the DEM difference and k_z obtained with the GAMMA software for the same acquisition.

B. Spatial and Temporal Analysis of DEM Time Series

To evaluate the spatial and temporal variability of elevation changes of Aletsch Glacier, we applied a pixelwise robust linear fit [59] to the winter acquisitions (October 1 to April 1) of the DEM time series. We limited the fit to winter acquisitions to avoid a bias from the higher availability of summer acquisitions in the first two observation years (2011 and 2012). Acquisitions with a very low height sensitivity ($h_{\text{amb}} > 1500$ m; see Fig. 2) were excluded from the analysis. The slope of the fit represents the annual height loss of the glaciers in the Aletsch region. As

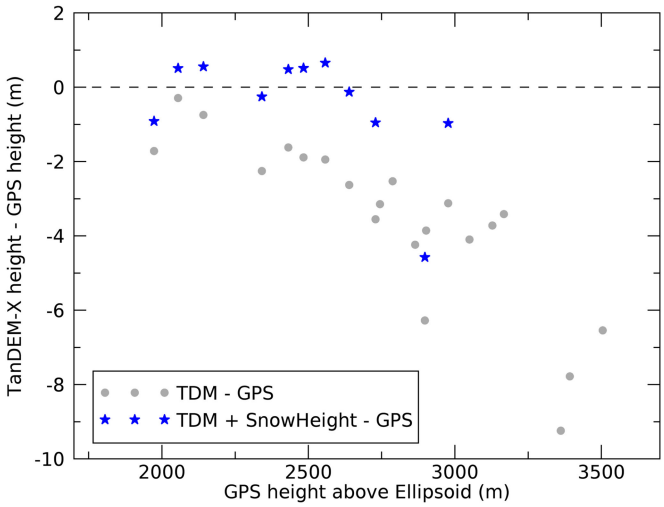

Fig. 7. Validation of the InSAR DEM of May 07, 2019 with GPS field measurements from May 06, 2019 and May 07, 2019. The InSAR DEM was corrected by field-measured snow heights over ice (blue asterisks). Gray dots indicate the difference to GPS heights without correction for snow penetration.

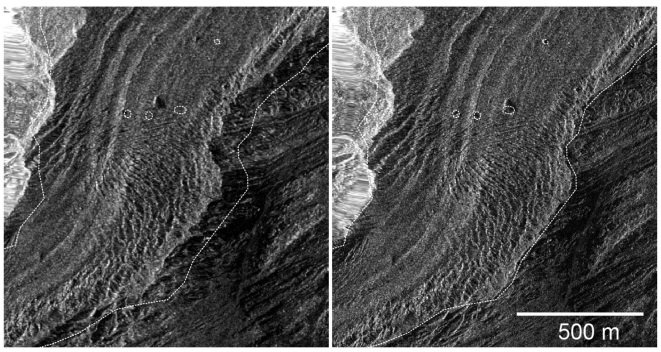

Fig. 8. Cross comparison of orthorectification of the scene from October 30, 2019 with features indicated by the white dotted line (lakes, glacier outline) derived from Sentinel-2 imagery from October 17, 2019. Left: orthorectification using the swissALTI3D; right: InSAR-based orthorectification using the TanDEM-X DEM from October 30, 2019.

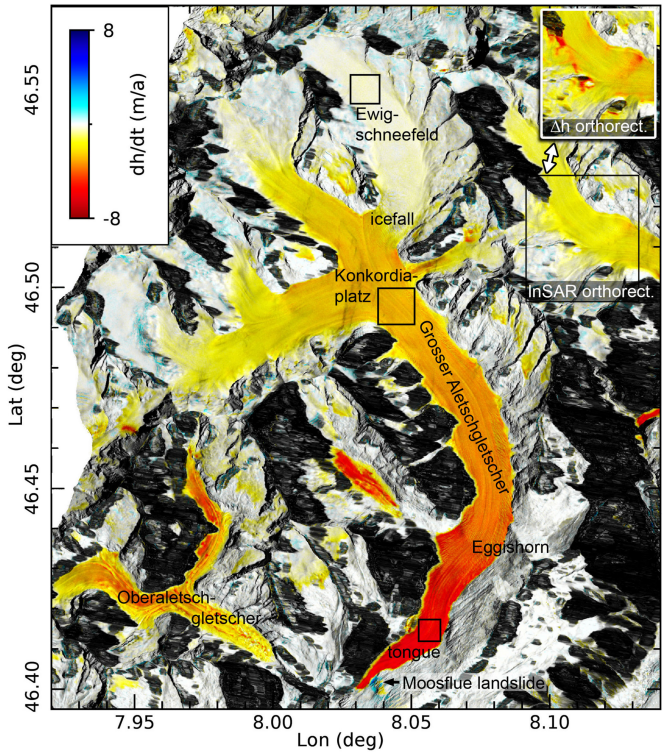

Fig. 9. Mean annual height change of Great Aletsch Glacier from InSAR-based orthorectification. Dark areas indicate low coherence due to radar layover or shadow. Height change time series of the three rectangles are presented in Fig. 11. In the lower left corner, Oberaletschgletscher is visible whose tongue is strongly debris covered. The inset in the upper right corner presents an example of artifacts on steeper terrain (red) originating from the orthorectification of DEM difference Δh_{res} without considering the correct geometry of Δh_{res} (Fig. 5).

the time series span 9 years, the bias from a varying penetration depth and from a seasonal height variability should be negligible.

For three representative locations, *Ewigschneefeld* in the accumulation zone (3350 m a.s.l.), *Konkordiaplatz* in the center of the glacier (2600 m a.s.l., 400 m below the long-term equilibrium-line altitude [60]), and on the *glacier tongue* (1950 m a.s.l.), we selected a square area of 800, 1000, and 600 m side length (Fig. 9). For these areas, we plotted DEM time series showing the cumulative average height loss relative to the height measured in the first observation year (2011). To obtain an estimate for the height accuracy within each area and for each acquisition, we calculated the standard deviation of the difference between each DEM and the temporal mean of all DEMs. As an indicator for dry and wet snow, we also calculated for each area the average backscatter signal (both polarizations HH and VV averaged). The threshold to distinguish between dry and wet snow was subjectively chosen about 2–4 dB below the winter backscatter signal.

To obtain elevation-dependent height change profiles for Great Aletsch Glacier and also for the smaller Oberaletschgletscher, we used the TanDEM-X DEMs between November 2015 and February 2016 to generate contour bands of each 10 m height. For each glacier, we generated a mask of the visible area. Then we calculated for each elevation band the mean height change and the corresponding standard deviation based on the data of the above described robust linear fit.

C. Analysis of the Velocity Fields

To generate an almost complete velocity field of Grosser Aletsch Glacier, we used all velocity maps generated with $\Delta t = 11$ d. From these maps, we calculated the componentwise (x, y) median for velocity vectors with a quality factor $q > 0.5$.

The success rate of velocity estimates by cross-correlation depends strongly on the persistence of trackable surfaces features. To study for which regions velocity estimates are most successful, we calculated the percentage of velocity estimates with a quality factor $q > 0.5$ for $\Delta t = 11, 22$, and 33 d.

To extract a seasonal variability of the velocity, we calculated monthly statistics over the two regions which showed the highest success rate of velocity estimates (Eggishorn, ice fall). The monthly statistics are based on the average acquisition time of each correlation pair and on the median velocity within each region of interest. For calculation of the median, we used only

velocity estimates with $q > 0.5$ and with time intervals between 22 and 44 d. The median window was 400×400 m (ice fall) and 300×300 m (Eggishorn) corresponding to 8×8 and 6×6 velocity samples.

To estimate a long-term trend in the velocity, we fitted a robust linear fit to all winter velocities (October 1 to April 1). We excluded summer velocities to avoid a bias as summer acquisitions exist only for 2011–2013.

To analyze how the two orthorectification methods (constant external DEM vs. up-to-date InSAR DEM, Section IV-A) affect velocity estimates, we compared the monthly velocity for each of the two generated image series.

D. Consideration of the HH and VV Polarization

To assess any possible height differences between the HH and VV InSAR DEMs, we analyzed for two representative areas, Konkordiaplatz and Ewigschneefeld (Fig. 9), the phase differences of the corresponding interferograms. As the mean phase difference over the two areas never exceeded 1°, we considered this difference to be negligible.

However, snow cover can strongly affect the polarimetric response, especially the copolar phase difference $\mathrm{CPD} = \varphi_{\mathrm{VV}} - \varphi_{\mathrm{HH}}$ [33]. Therefore, we calculated time series of the CPD, the copolar coherence $\gamma_{\mathrm{VV,HH}}$, and the HH/VV backscatter ratio $\sigma_{\mathrm{HH}}/\sigma_{\mathrm{VV}}$ for the two sites. To obtain a positive correlation between between $\gamma_{\mathrm{VV,HH}}$ and the backscatter ratio, we calculated the ratio HH/VV instead of VV/HH. For calculation of the CPD, the backscatter alignment convention causes a 180° phase shift when calculated for the receive-only satellite in a bistatic acquisition pair [33, Section 3.3]. Therefore, we calculated the CPD from the data of the bistatic transmitter.

The variability of the CPD can be difficult to interpret, but recent modeling shows a good agreement with both radar and computer tomographic measurements [35]. They show that snow settling after snow fall causes horizontal structures in the snow pack driving the CPD toward positive values, whereas a vertical temperature gradient causes metamorphism of the ice grains toward a preferentially vertical orientation driving the CPD toward negative values. Because of these findings, positive changes of the CPD can be used as a proxy for snow accumulation. For that, we calculated the cumulative sum of positive phase differences from October 1 to end of May

$$\Sigma\Delta\mathrm{CPD}^{+} = \sum_{i \in \mathrm{Oct–May}} \max\left(\mathrm{CPD}_i - \mathrm{CPD}_{i-1}, 0\right) \qquad (19)$$

and compared $\Sigma\Delta\mathrm{CPD}^{+}$ with the cumulative sum of the monthly winter precipitation.

VI. Results

A. Validation of DEMs and InSAR-Based Orthorectification

The comparison of the TanDEM-X heights to the GPS measured heights in Fig. 7 shows that the TanDEM-X heights underestimate the GPS heights by several meters (gray bullets). However, the difference is close to zero when the InSAR DEM is corrected by the snow height measured in the field (blue asterisks). The root mean square error (RMSE) between snowdepth-corrected TanDEM-X heights and field measurements is 1.5 m. For most of the uncorrected elevations above Konkordiaplatz (>2700 m), the TanDEM-X heights are up to 10 m below the GPS heights which we attribute to microwave penetration into the firn in the accumulation zone. There, the snow depth exceeded the length of the avalanche probe (2.6 m) and could therefore not be measured.

For validation of the orthorectification, we compared two orthorectified radar backscatter images of the glacier tongue (Fig. 8), acquired on October 30, 2019 with features extracted from a Sentinel-2 image (October 17, 2019, $\theta = 4.5°$). As expected, when using the outdated swissALTI3D from 2009, horizontal shifts of 80–100 m appear. In contrast, the InSAR-based orthorectification shows only shifts on the resolution level of Sentinel-2 (10–20 m).

In the comparison to results obtained using the GAMMA software, we found a systematic (but for our study, negligible) deviation of $1.3 \pm 0.015\%$ for k_z. As the source code of the GAMMA software is not available to us, we can only speculate that the deviation might result from the fact that we halved the distance of the orbit state-vector (bistatic receiver and bistatic transmitter) in the baseline parameter file of our processing pipeline originally designed for monostatic interferograms. For the height difference in radar coordinates, we obtained very comparable results (RMSE: 1.5 m for height differences reaching up to 50 m). To avoid horizontal shifts in mountainous terrain (Fig. 5) causing artifacts like shown in the inset of Fig. 9, it seems important to us to transform the InSAR-based height (in slant-range coordinates) correctly into map coordinates by updating the orthorectification lookup table using the GAMMA function gc_insar.

B. Average Elevation Loss

From the large number of elevation models, we obtained a map of the mean annual elevation change by pixelwise regression (Section V-B), shown in Fig. 9 for the period between 2011 and 2019. The figure was overlaid with the mean coherence of all interferometric pairs. Dark areas indicate regions with low coherence which are mainly areas affected by layover or radar shadow. Aletsch Glacier shows the strongest elevation loss of about 6–8 m a^{-1} over the very end of the tongue. For the area average, we obtained an elevation loss of 1.54 m a^{-1} over the total observed area of 59 km^2, corresponding to a total volume loss of $91 \times 10^6\ \mathrm{m}^3\mathrm{a}^{-1}$ in this area.

Fig. 10 shows the elevation-dependent height loss of Great Aletsch Glacier and of Oberaletschgletscher. The height loss profile of Aletsch Glacier is characteristic for a glacier which experiences strongly imbalanced conditions due to strongly increased surface melt at elevations below 3200 m. Reduced precipitation can be excluded as above 3200 m, the annual mass balance is close to zero. In contrast to Aletsch Glacier, the height loss of Oberaletschgletscher on its tongue (between 2150 and 2400 m) is almost half of that of the area area above (between 2400 and 2700 m). From field visits and satellite imagery, we know that the tongue of Oberaletschgletscher is strongly debris covered, while the tongue of Aletsch Glacier exposes mostly bare ice causing stronger melt. Therefore, we attribute the reduced height loss to the insulating effect of debris covered on the tongue of Oberaletschgletscher.

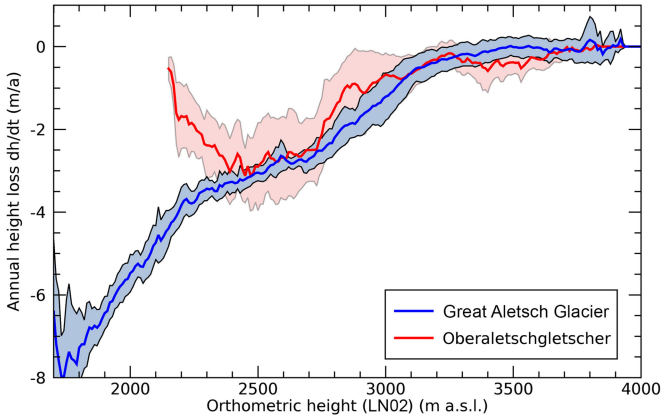

Fig. 10. Elevation-dependent height loss of Great Aletsch Glacier and Oberaletschgletscher calculated for 10 m elevation bands (solid line) with standard deviation (thin lines). Oberaletschgletscher (red) shows a reduced elevation loss below 2400 m due to debris covered on its tongue.

In Fig. 11, we observed a cumulative elevation loss of about 2.5 m in the upper accumulation area (Ewigschneefeld, 3350 m), about 30 m at Konkordiaplatz, and almost 60 m at the glacier tongue within the 9 years between 2011 and 2019. The annual height loss for the three sites, given in Fig. 11, is also indicated by the dashed line (robust linear fit). All three sites show an accelerated height loss as indicated by the negative curvature of the dotted line (second-order polynomial fit).

C. Seasonal Variability

Fig. 11 shows a strong seasonal height variability with an apparent height loss of over 10 m during summer and a similar height gain in spring. Interestingly, the minimum height is reached every year between December and January (vertical gray dashed lines) which is already in the middle of the accumulation period (October–May, gray shading in Fig. 11). The reason is the penetration of microwaves into the snow which is freezing progressively below the summer surfaces. This is supported by the abrupt increase of the interferometric phase center in spring (green elevation dots in Fig. 11) which result from the negligible microwave penetration depth into wet spring snow compared to the dry winter snow. Wet snow (green dots) was detected when the radar backscatter intensity drops below the winter signal (the dashed line in the lower panels of Fig. 11 shows threshold values).

D. Penetration Depth Into Dry Snow

When a cold, dry snow pack suddenly starts to melt, the increase of the interferometric phase center can be used to estimate the penetration depth of X-band microwaves into dry snow. For example, in April 2013, a series of three TanDEM-X acquisitions with a sufficiently small h_{amb} of 61, 81, and 133 m captured the onset of snow melt during which temperatures increased by +10 K with little precipitation [Fig. 12(b)]. The two meteostations BLA and FIT measured in average about 30 mm precipitation between each two of the acquisitions, corresponding to 15 cm of snow at a snow density of 0.2 g cm^{-1}. As precipitation does not increase significantly with elevation in the Alps [39], the height bias due to fresh snow should be

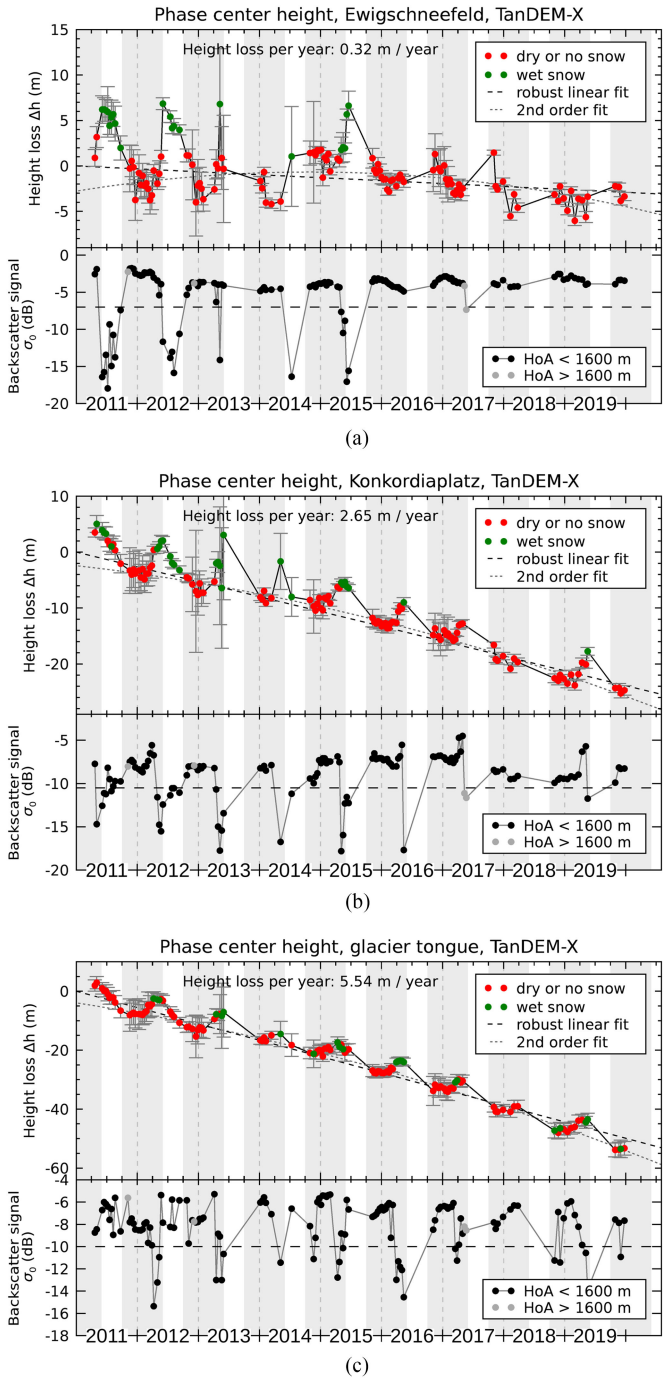

Fig. 11. Evolution of the interferometric phase center height at three selected locations: Ewigschneefeld (3350 m), Konkordiaplatz (2600 m), and the glacier tongue (1950 m). In the upper panels, the dashed line indicates a robust linear fit to winter acquisitions (October 1 to April 1); the dotted lines indicate a second-order polynomial fit. The backscatter signal in the lower panels shows distinct dips during snow melt for which the phase center reaches the highest value every season (green dots). Gray dots indicate backscatter values for which height values are not shown because of a very large HoA $>$ 1600 m. The gray shading indicates the winter season from October 1 to June 1.

negligible compared to the height change of 2–6 m observed in Fig. 12(c). The height between April 6, 2013 and April 17, 2013 increases with elevation up to a mean height change of 4 m. For higher elevation above 3300 m, the height change decreases as the snow surface remained partially dry here. This is indicated

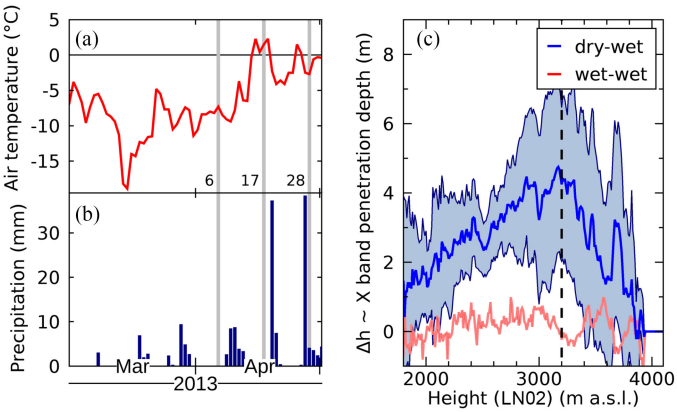

Fig. 12. In spring 2013, the onset of snow melt was captured by three TanDEM-X acquisitions (April 6, 17, and 28) indicated by gray bars in (a) and (b). During the first two acquisitions, the temperature increased by +10 K leading to surface melt over major parts of the glacier. The elevation difference observed at the transition from dry to wet snow conditions, blue in (c), can be interpreted as a change in penetration depth (blue line: mean height change per elevation band; blue area: standard deviation). The black dashed line indicates a height of 3200 m below which the backscatter signal dropped by more than 2 dB indicating the transition from dry to wet snow. The red line indicates the height difference between the later two acquisitions which both had wet snow conditions.

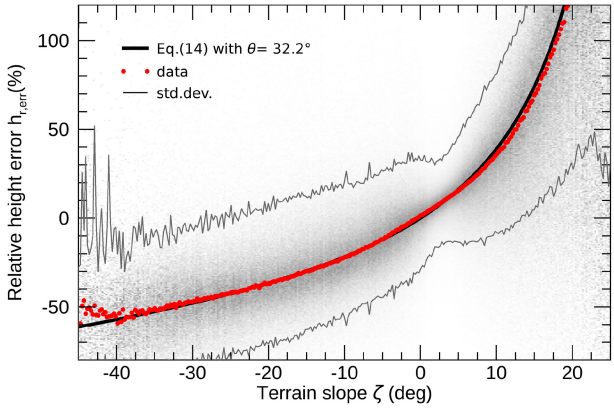

Fig. 13. Significant height error occurs when the slant-range radar geometry is not considered during orthorectification of Δh_{res} measured in radar coordinates. The terrain slope ζ is measured in the slant-range plane (see Fig. 5).

by the vertical black dashed line in Fig. 12(c) which indicates the elevation above which the backscatter between April 6, 2013 and April 17, 2013 remained fairly constant and dropped less than 2 dB. Below the dashed line, the backscatter intensity dropped up to 8 dB.

For comparison with these results, we also analyzed the later acquisition pair of April 17, 2013 and April 28, 2013 during which temperatures remained warm and about 30 mm precipitation fell again. The red curve in Fig. 12(c) shows that the elevation-dependent height change is close to zero (area-mean of +0.23 m). As snow conditions did not change much between the second and third acquisitions, we attribute the entire height change between April 6 and 17 to penetrate into snow.

E. Height Change in Radar Coordinates vs. Map Coordinates

In Section III-H about the InSAR-based orthorectification, (15) describes the relative height error $h_{\text{r,err}}$ which results when the slant looking geometry is not considered during orthorectification of the height change Δh_{res} measured in radar coordinates. To assess the validity of (15), we calculated $h_{\text{r,err}} = (\Delta h_{\text{res}} - \Delta h_{\text{true}})/\Delta h_{\text{true}}$ using, for Δh_{true}, the data shown in Fig. 9 (InSAR-based orthorectification) and for Δh_{res}, the corresponding data without considering the slant looking geometry (shown in the inset of Fig. 9). Fig. 13 shows that relative height errors $h_{\text{r,err}}$ larger than 10% occur already for terrain slopes $|\zeta| > 5°$ and that the error increases quickly above 50% for slopes facing the radar ($\zeta > 0$). The error diverges to infinity when ζ approaches the radar incidence angle θ (transition to layover). Fig. 13 highlights the importance of a correct InSAR-based orthorectification of radar DEM differences.

F. Baseline Dependence of Coherence

For InSAR DEMs, the vertical precision generally increases when the height of ambiguity h_{amb} decreases. However, when

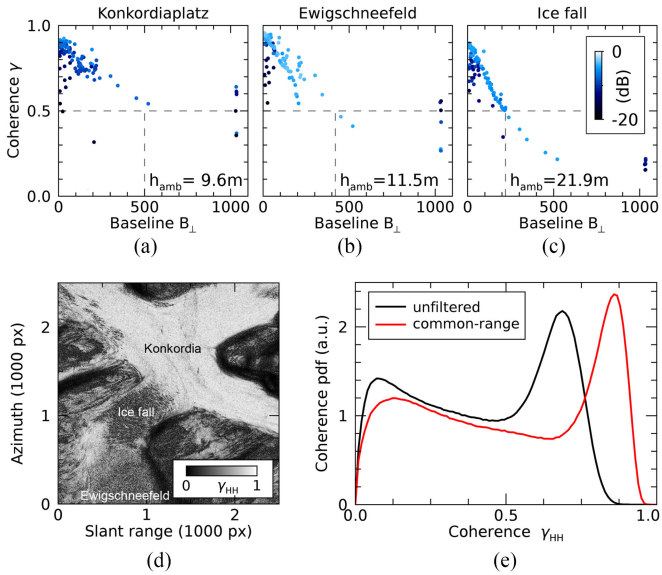

Fig. 14. (a)–(c) Decay of interferometric coherence (average of γ_{VV} and γ_{HH}) for increasing baselines at three different sites with different snow and ice conditions. For Konkordiaplatz, (a) up to 4 m of snow accumulate over bare ice in winter. Ewigschneefeld (b) is located in the accumulation zone with deep firn. The ice fall (c) is dominated by large and deep crevasses covered by a few meters of snow. Dots are colored according to the backscatter intensity σ_0. (d) Coherence image after range common-band filtering for the large baseline acquisition on April 24, 2015 ($B_\perp = 1032$ m). (e) Coherence histogram of the data shown in (d) for unfiltered and range common-band filtered coherence.

h_{amb} is too small, a significant loss of coherence can occur. Fig. 14 shows the dependence of the interferometric coherence on the effective baseline for three different sites. At Konkordiaplatz [Fig. 14(a)], the coherence is above 0.5 for all baselines smaller than 500 m ($h_{\text{amb}} > 9.6$ m). Konkordiaplatz is covered by 2–4 m of snow in winter and is ice-free in summer so that little volume decorrelation occurs. For Ewigschneefeld, covered by deep firn in the accumulation area, the surface melts every summer but refreezes such that cold firn can exist to a depth of around –15 m [61]. Here, the coherence decays slightly faster [Fig. 14(b)] and drops below 0.5 for $B_\perp > 420$ m ($h_{\text{amb}} < 11.5$ m). At the ice fall where the glacier Ewigschneefeld drops

down to Konkordiaplatz [Fig. 14(d)], very large and deep crevasses exist. Due to this strong topographic variations, the coherence in Fig. 14(c) drops already below 0.5 for $B_\perp > 220$ m ($h_{\text{amb}} < 21.9$ m). This is much smaller than the critical baseline $B_{\text{crit}} = 5.7$ km [see (17)] for which even perfectly flat terrain shows a complete coherence loss. These results illustrate that for DEM generation of glaciers, the amplitude of short-range topographic variations is very relevant and baselines with a very small h_{amb} do not provide meaningful height information. In agreement with [22], we think that h_{amb} less than 20 m are not of advantage for glacier monitoring.

G. Range Common-Band Filtering

To improve the coherence of the large baseline acquisitions in spring 2015, we applied the range common-band filter described in Section III-K. The large effective baselines of $B_\perp = 1034\,\text{m}$ are at 18% of B_{crit}, (17), resulting in a strong reduction of the coherence. Fig. 14(d) shows a coherence image of Konkordiaplatz after range common-band filtering; Fig. 14(e) shows the corresponding histogram of the unfiltered and filtered coherence. Over Konkordiaplatz, we obtained an coherence increase by +0.15 from 0.68 to 0.83 with the topography-adaptive filtering method described in Section III-K.

H. Velocity Maps

The median velocity of Great Aletsch Glacier for the period 2011–2019 is shown in Fig. 15 on top of the backscatter intensity. The shown velocity was derived from backscatter data orthorectified with the swissALTI3D. At the steepest part of the glacier, at the ice fall, the velocity reaches up to 0.8 m d^{-1}. Below Konkordiaplatz, the maximum velocity is 0.4 m d^{-1}, and near Eggishorn, the velocity is 0.29 m d^{-1}. Contour lines indicate velocity intervals of 0.05 m d^{-1}.

The success of intensity tracking depends on the visibility of trackable features. Fig. 16 shows that for $\Delta t = 11\,\text{d}$, only the glacier tongue near Eggishorn and the ice fall, where large crevasses are present, could be tracked with almost all of the 89 available image pairs. In contrast, in the accumulation area at Ewigschneefeld, where deep smooth firn is present, only 5%–10% of image pairs lead to successful velocity estimates. In average, we obtained for 86% of the entire area, reliable results with a quality $q > 0.5$. When increasing the time interval to $\Delta t = 22$ and 33 d, we still obtained in average 81% and 77% of successful velocity estimates.

Of the entire analyzed time series, the image pair of November 17, 2011 and November 28, 2011 showed, by far, the best correlation and a coverage of 92%. November 2011 was the driest November since over 150 years and no precipitation fell in entire Switzerland between November 9, 2011 and November 30, 2011 [62]. This image pair even has a reasonable 11-d repeat-pass coherence (not shown) over several parts of the glacier which could even allow for coherence tracking or speckle tracking [36] in the accumulation zone above the ice fall.

I. Validation of Velocity Measurements

The validation of the annual median velocity field (2011–2019), Fig. 15, with the field data from May 2019 shows a good correlation with an RMSE of 0.04 m d^{-1}. Summer acquisitions show a stronger scatter, but only a few summer acquisitions were available. Shows a good correlation with an RMSE of 0.04 m d^{-1} (Fig. 17)

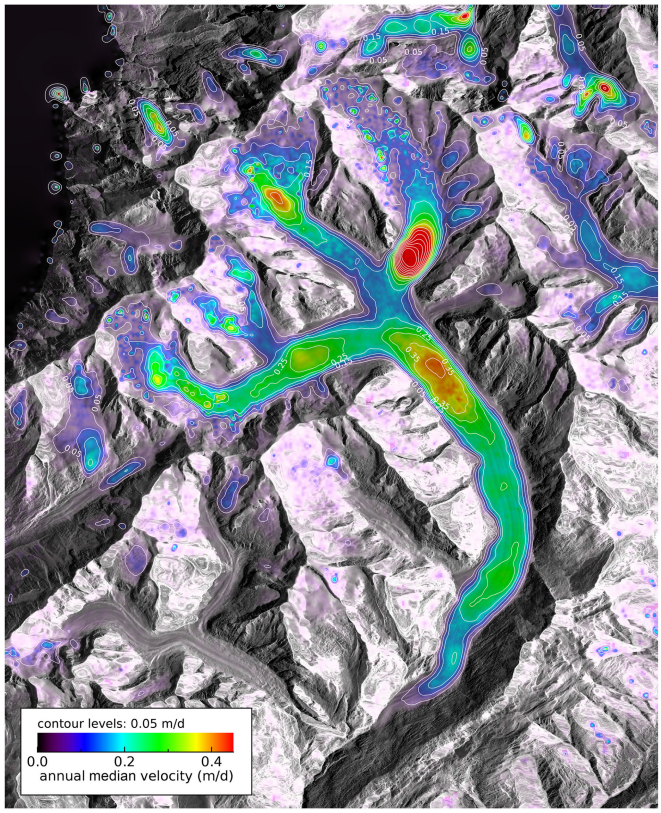

Fig. 15. Median velocity of Great Aletsch Glacier and adjacent glaciers from offset tracking using 89 TanDEM-X intensity image pairs with 2 m resolution, $\Delta t = 11$ d, a patch size of 96 × 96 pixels, and a quality threshold $q > 0.5$.

J. Seasonal Velocity Analysis

For the two locations, the glacier tongue near Eggishorn and the ice fall, almost all image pairs achieved successful velocity estimates (black boxes in Fig. 16). Therefore, we used these two locations to analyze the two generated sets of velocity times series, once obtained from backscatter images orthorectified using the swissALTI3D (gray dots in Fig. 18) and once using the InSAR-based orthorectification described in Section IV-A (black dots in Fig. 18). At first glance, both datasets show very similar results [Fig 18(a)]: At the ice fall, we observe a mean velocity of 0.61 ± 0.04 m d^{-1}. At Eggishorn, the mean velocity is 0.29 ± 0.04 m d^{-1}. At the ice fall, a robust linear fit to the 9 years of winter acquisitions (October 1 to May 1) indicates a velocity decrease of –5.0 mm d^{-1} a^{-1} and for Eggishorn, we obtain a velocity decrease of –5.9 mm d^{-1} a^{-1}.

At second glance, when looking at the monthly mean velocities [Fig. 18(b) and (c)], both locations show that the summer velocity is about 0.1 m d^{-1} higher than winter velocities. However, the speedup in spring is less pronounced for the InSAR-based orthorectified image series (black symbols), compared to the orthorectification using the constant swissALTI3D (gray symbols) for which the lowest velocities are observed in March and April

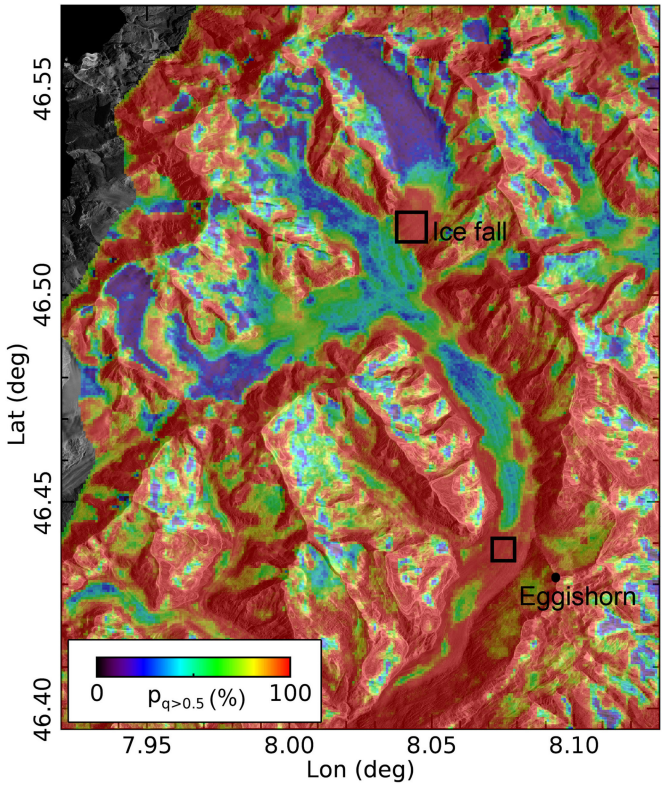

Fig. 16. Probability p (in %) for successful velocity tracking using 89 image pairs with $\Delta t = 11$ d. In contrast to the ice fall and the glacier tongue, where crevasses are visible all year, the velocity of the accumulation area at Ewigschneefeld can only by tracked by 5%–10% of all image pairs.

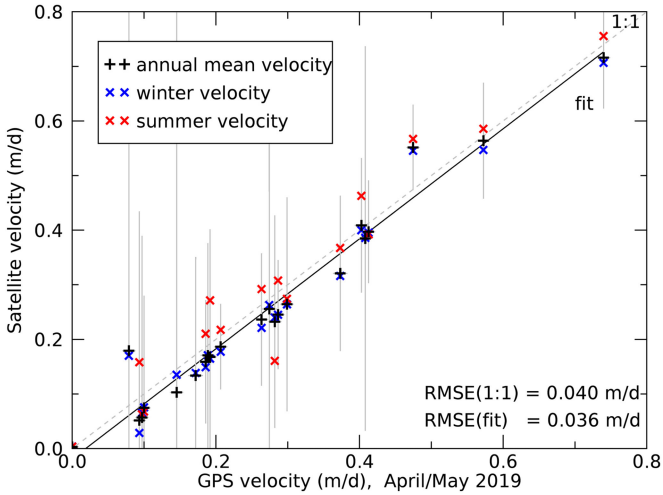

Fig. 17. Validation of the median satellite velocity data from Fig. 15 ($\Delta t = 11$ d) using GPS data acquired between April 30, 2019 and May 7, 2019 at the 23 locations shown in Fig. 1 and listed in Table II. Gray lines indicate the velocity standard deviation.

(at the onset of snow melt) and the highest velocity in June/July during snow melt. The reason for this discrepancy is the dynamic of the observed surface height (i.e., of the interferometric phase center) which appears closer to the radar at the onset of snow melt (transition from dry snow to wet snow) resulting in an apparent velocity bias toward the radar. During snow and ice melt in summer, the observed height moves away from the radar

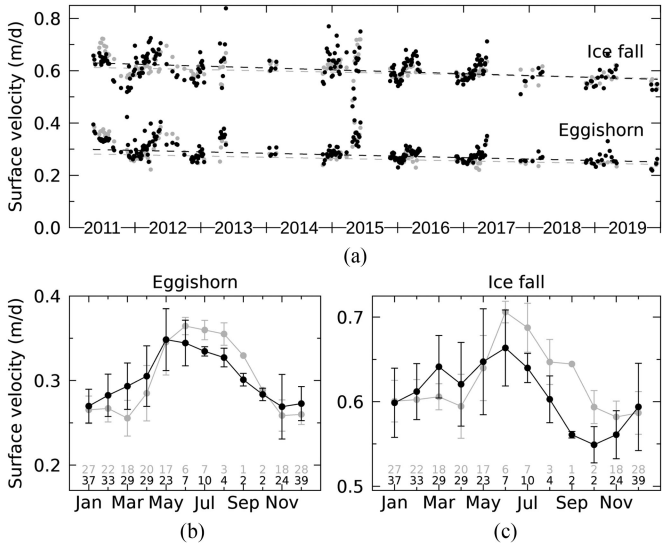

Fig. 18. (a) Velocity time series for Eggishorn and for the ice fall. Gray data points are velocity estimates using the constant swissALTI3D for orthorectification; black data points are velocity estimates using dynamic InSAR-based orthorectification. (b), (c) Seasonal velocity variations at the two locations. Numbers indicate the number of acquisition pairs used to compute the monthly mean velocity; error bars indicate the standard deviation.

causing an apparent increase of the velocity in the ground range direction (toward west for our descending acquisitions). The lowest velocity for the ice fall are observed in October. The comparison of the two velocity datasets in Fig. 18(b) and (c) highlights that variations of the microwave penetration and surface height can significantly bias monthly SAR velocity estimates, whereas InSAR-based orthorectification using TanDEM-X data can provide trackable 3-D backscatter point clouds that allow for generation of unbiased velocity estimates. The bias is only significant when the height variations of the phase center are not negligible compared to the horizontal displacement. Therefore, phase center height variations affect mainly monthly velocity estimates but little annual mean velocities.

K. Correlation Between Snow and HH and VV Polarization

Fig. 19 shows time series of the CPD, the copolar coherence $\gamma_{VV,HH}$, the backscatter ratio σ_{HH}/σ_{VV}, and the cumulative CPD according to (19) together with monthly and seasonal mean temperatures and precipitation. As already observed in [33] and [34], the CPD is close to zero in summer [Fig. 19(a)] when microwaves do not penetrate the wet snow cover (Ewigschneefeld, red) or the bare ice (Konkordiaplatz, black). In winter, the CPD increases with snow fall and peaks during or after months with the most intense precipitation. Temperature gradient metamorphism [35] and snow melt decrease the CPD signal. As an increasing CPD correlates with fresh snow [34], we plotted the cumulative CPD $\Sigma\Delta\text{CPD}^{+}$ [see (19)] together with the cumulative precipitation (scaled by a factor of 0.15) and obtain similar trends at least in seasons where the acquisition time series do not show large temporal gaps (e.g., winter 2013/2014). These reasonably similar trends provide a simple mean to estimate the snow accumulation, even though we did not consider any underlying processes of snow metamorphism [35] which depend mainly on the temperature gradients in the snow pack. Also, we

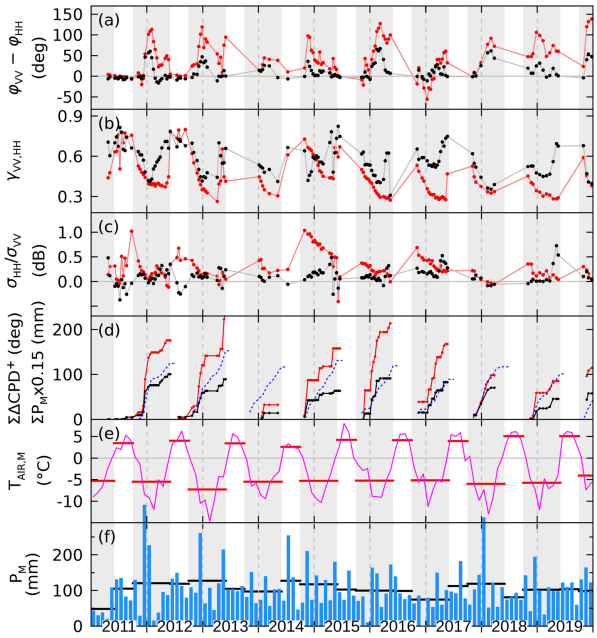

Fig. 19. Sensitivity of dual-pol data to snow conditions in winter (October1 to June 1, gray shading) and summer (no shading) for Ewigschneefeld (red dots) and Konkordiaplatz (black dots). (a) CPD increases temporarily with snowfall but decreases during periods of dry and cold weather due to temperature gradient metamorphism [35]. (b) Copolar coherence $\gamma_{VV,HH}$ decreases every winter due to increased penetration into snow and firn where volume scattering occurs. (c) HH/VV backscatter ratio is very close to unity (0 dB) but shows some correlation with $\gamma_{VV,HH}$. (d) Cumulative, positive temporal changes of the CPD roughly correlate with the cumulative amount of dry precipitation (dotted blue line) in winter. (e) Monthly mean air temperature and (f) monthly precipitation; horizontal bars indicate the summer (June–September) and winter (October–May) mean air temperature and precipitation.

did not consider CPD changes due to varying penetration which could provide a considerable potential to improve estimations of snow accumulation based on the CPD. For example, the CPD close to zero in spring 2013 [Fig. 19(a)] for Ewigschneefeld results from the transition from dry to wet snow analyzed already in Section VI-D. This transition is indicated in Fig. 19(b) by the peak in copolar coherence indicating low penetration and also by drop of the absolute backscatter in Fig. 11(b) indicating wet snow.

The shown CPD was derived from the monostatic satellite (active transmitter of TanDEM-X). For the CPD from the receive-only satellites (bistatic, passive receiver), we observed the expected 180° phase shift (Section V-D) but surprisingly only for acquisitions between 2011 and 2016. In 2017, the expected phase shift between both satellites disappeared.

The copolar coherence is around 0.6,...,0.8 during summer and snow melt where mainly surface scattering occurs, but it decreases to 0.3 in winter by increasing volume scattering. The HH/VV backscatter ratio is small. It increases in early winter by 0.5–1 dB but decreases during the remaining winter.

VII. Discussion

A. Ice Loss in a Warming Climate

Like all glaciers in the European Alps Aletsch Gletscher is strongly retreating while air temperatures are rising especially in the higher mountains. The annual area mean temperature for northern Switzerland above 1000 m a.s.l. [63], [64] were 2.3 °C above preindustrial temperatures during our study period (2011–2019). In our TanDEM-X dataset, we have observed an elevation loss between –8 y^{-1} on the tongue at 1700 m a.s.l. which gradually decreases to –1 y^{-1} on 3000 m indicating a strongly imbalanced state. For all elevation zones, we observed an accelerated ice loss based on elevation models from nine winter seasons. A study from 2011 [37] provides simulations of the future evolution of Great Aletsch Glacier which show different height loss rates depending on the chosen climate scenario. However, a more recent study from 2019 [38] found a remarkable agreement between simulation results of the median, the most, and the least glacier friendly climate scenario until 2050; however, they also found a strong spread afterwards until 2100 ranging between 60% and almost complete loss of the entire ice mass. Due to the remarkable agreement between simulations, we consider our observation period 2011–2019 as too short to draw substantial conclusions which of the used scenarios matches best.

B. Optimal InSAR Acquisitions for Glaciological Applications

SAR missions like TerraSAR-X can provide high-resolution imagery well suited for velocity tracking. Flying in a bistatic formation, the TanDEM-X InSAR mission can additionally provide time series of elevation models allowing for observations of the dynamics of surface elevation changes. However, varying surface properties resulting in different penetration depths make interpretation of DEMs acquired on a single date difficult. In this study, we observed penetration depths of 2–6 m in the accumulation zone at about 3300 m a.s.l. Several methods have been proposed to estimate this penetration depth based on correlations between penetration, backscatter signal, and interferometric coherence; see, e.g., [18] and [19]. In our polarimetric dataset, we observed that also the copolar coherence $\gamma_{VV,HH}$ shows a seasonal dependence which could provide an additional parameter to estimate the penetration depth. The copolar phase, in contrast, varies strongly with snowfall and temperature [35] and seems not to be useful for penetration estimates. Nevertheless, it can be used as a proxy for snow accumulation when dense enough time series with repeat interval not much larger than 11 d are available [33].

For estimation of the multiyear trend of surface height changes, single-pass InSAR DEM time series can provide precise estimates when a sufficient number of acquisitions is available. Despite penetration, in our DEM time series analysis, the surface height seems to be most stable in winter. Therefore, we think that multiyear time series consisting of winter acquisitions could provide the most reliable long-term radar height change estimates, whereas acquisitions in spring, which would better agree with the end of the ablation period, are most strongly affected by snow-melt related height changes.

Winter acquisitions over glaciers have the additional advantage that the snowpack is very likely dry. Therefore, the backscatter signal is higher above the noise floor which increases the interferometric coherence and therefore simplifies DEM generation. To avoid coherence loss due to a strongly variable topography (e.g., crevasses), ambiguity heights larger than $h_{amb} \approx 20$ m are favorable (for TanDEM-X: $B_\perp < 200$ m). For

the best height precision, baselines should not be much smaller because a phase noise of 2° would correspond to an height noise of 11 cm at $h_{\text{amb}} = 20$ m. While our study benefits from the large variety of baselines, DEM generation and estimation of imaging-geometry dependent height bias would benefit from relatively constant baselines [25].

C. Slant Geometry for DEM Difference Orthorectification

Even though correctly explained in [42] and [43], it seems to be a common misunderstanding that InSAR DEM differences measured in radar coordinates can simply be orthorectified using an external reference DEM. However, the observation of DEM differences with respect to the external reference DEM directly indicates that distortions will occur during orthorectification. These distortions can be calculated explicitly as suggested by (14). In Fig. 5, we have illustrated how to correctly update an existing point P on the reference DEM by a new point P_{new}. The inset of Fig. 9 shows how height artifacts (in red) appear at terrain slopes, especially when facing the radar, in comparison to the main figure where such artifacts are absent. In Fig. 13, we have shown a quantitative analysis of the relative height error which occurs when the slant geometry of DEM difference observed in radar coordinates is not correctly considered during orthorectification. In this work, we provide a method to correctly consider the DEM difference geometry. Artifacts in height changes can not only lead to wrong conclusions when analyzing DEM difference but can also propagate into glacier models when incorrectly processed InSARs are used as input data. We, therefore, strongly suggest to validate InSAR processing chains, e.g., by reconstructing artificial height changes added to reference DEMs on nonhorizontal terrain.

D. Velocity Bias Due to Height Changes

For velocity estimates, the slant imaging geometry of SAR sensors can provide a significant problem when the DEM used for orthorectification is outdated. Because of the seasonal dynamic of the glacier surface height, any DEM that was not acquired instantaneously with the SAR images is outdated—even for a glacier with a stable mass balance. Due to the slant viewing geometry of SAR sensors (and possibly others), surface height variations result in horizontal shifts in the orthorectified images which can be misinterpreted as a velocity signal. For example, in our case, the DEM time series indicate an elevation loss of about 10 m within 6 months (April–September). For the data acquired from a descending orbit and an incidence angle of $\theta = 32°$, this elevation loss could be misinterpreted as a horizontal shift of 20 m toward west resulting in a velocity bias of 0.11 m d^{-1} during summer. Similarly, the transition from dry to wet snow, appearing as a positive elevation gain of several meters, could be misinterpreted in our first dataset (orthorectified with the external DEM) as a shift toward east resulting in a negative velocity bias in spring. Using the InSAR-based orthorectification for our second velocity dataset, we were able to observe this velocity bias in Fig. 18 and found velocity shifts in the expected range of 0.05–0.1 m d^{-1}. Our monthly velocity analysis shows, in agreement with the DEM time series (Fig. 11), that winter velocities can be most reliably measured because, in winter, the height of the interferometric phase center appears most stable.

VIII. Conclusion

In this article, we presented and analyzed a large TanDEM-X data set acquired of the Great Aletsch Glacier that was defined as a TanDEM-X super testsite for glaciological applications. Using our own code for DEM generation, we calculated time series of elevation models from the provided CoSSC data. We highlighted a common pitfall for InSAR DEM generation and provide a method for explicit DEM generation avoiding time-consuming iterative methods to improve an auxiliary reference DEM. We implemented an InSAR-based orthorectification to generate 3-D radar backscatter point clouds from interferometric TanDEM-X acquisitions. With that, we demonstrated that the derived TanDEM-X DEM of each acquisition can be used to generate orthorectified radar images which are not distorted by an outdated DEM.

We analyzed the spatial and temporal loss of ice height, analyzed the penetration depth into dry snow, and suggested an optimal height of ambiguity for DEM generation over glaciers. We interpreted dual polarimetric time series (HH and VV) with respect to seasonal snow metamorphism, snow accumulation, and radar penetration.

We generated an almost complete surface velocity map of Great Aletsch Glacier and observed that the seasonal surface velocity derived from SAR data can be significantly biased by seasonal surface height changes caused by penetration change or ice melt. The suggested InSAR-based orthorectification avoids such a velocity bias.

We conclude that InSAR time series of glaciers are most useful when acquired in winter. Reasons are the higher signal-to-noise ratio and the slower vertical dynamics of the height of the interferometric phase center compared to spring where a variable penetration depth makes surface height change estimates difficult. In summer, the surface elevation changes much faster due to ice melt, whereas, in winter, the surface elevation appears relatively stable as microwaves penetrate the fallen fresh snow. Similar to [33] and [34], we found that positive changes of the copolar phase can be used as a proxy for snow accumulation. The copolar coherence could help to improve estimates of the radar penetration depth. We further conclude that seasonal height changes can significantly affect SAR velocity estimates when the height changes are not considered during orthorectification. With this study, we like to point out the uniqueness and the importance of bistatic InSAR mission like TanDEM-X and presented therefore a collection of results which are applicable for glaciological applications world wide.

Acknowledgment

The authors would like to thank Thomas Busche for his excellent support regarding technical details and the acquisition service of TanDEM-X. They also thank Alexandra Kuhn for an excellent B.Sc. thesis about the surface velocity of Aletsch Glacier. They thank the two anonymous reviewers for their valuable suggestions to improve the article. The TanDEM-X data used in this study was provided by the German Space Agency DLR via proposal XTI_GLAC6780. Meteorological and climate data was provided by the Swiss Federal Office of Meteorology and Climatology MeteoSwiss by the dataportals IDAweb and CLIMAP-net.

Author contributions: S. Leinss developed the algorithms and methods, processed and analyzed the data, and wrote the article. P. Bernhard did the processing with the GAMMA software. S. Leinss and P. Bernhard did the GPS measurements and discussed the interferometric processing methods.

Data set: Generated DEMs and velocity maps are available in the ETH research collection. DOI: 10.3929/ethz-b-000482456.

References

[1] A. Bauder, M. Funk, and M. Huss, "Ice-volume changes of selected glaciers in the Swiss Alps since the end of the 19th century," *Ann. Glaciol.*, vol. 46, no. 1, pp. 145–149, 2007.

[2] D. Farinotti, M. Huss, A. Bauder, and M. Funk, "An estimate of the glacier ice volume in the Swiss Alps," *Glob. Planet. Change*, vol. 68, no. 3, pp. 225–231, 2009.

[3] V.-E. Zurich, "Glaciological reports. 1881–2015. The Swiss Glaciers, 1889–2014/15," *Yearbooks of the Cryospheric Commission of the Swiss Academy of Sciences (SCNAT)* 1–245, Published since1964.

[4] GLAMOS 1881–2019, "The swiss glaciers 1880–2016/17," Yearbooks of the Cryospheric Commission of the Swiss Academy of Sciences (SCNAT), Published since 1964 by VAW/ETH Zurich, *Glaciological Rep.*, 2016. [Online]. Available: http://swiss-glaciers.glaciology.ethz.ch/data/aletsch.html

[5] M. Zink, G. Krieger, H. Fiedler, and A. Moreira, "The TanDEM-X mission: Overview and status," in *Proc. IEEE Int. Geosci. Remote Sens. Symp.*, 2007, pp. 3944–3947.

[6] G. Krieger *et al.*, "TanDEM-X: A radar interferometer with two formation-flying satellites," *Acta Astronaut.*, vol. 89, pp. 83–98, 2013, doi: 10.1016/j.actaastro.2013.03.

[7] S. Vijay and M. Braun, "Seasonal and interannual variability of Columbia Glacier, Alaska (2011–2016): Ice velocity, mass flux, surface elevation and front position," *Remote Sens.*, vol. 9, no. 6, pp. 1–18, 2017, Art. no. 635. doi: 10.3390/rs9060635.

[8] E. Maurer, R. Kahle, F. Mrowka, G. Morfill, A. Ohndorf, and S. Zimmermann, "Operational aspects of the tandem-x science phase," in *Proc. SpaceOps Conf.* Amer. Instit. Aeronautics Astronaut. Inc., 2016, pp. 1–18.

[9] P. Rizzoli *et al.*, "Generation and performance assessment of the global TanDEM-X digital elevation model," *ISPRS J. Photogramm. Remote Sens.*, vol. 132, pp. 119–139, 2017.

[10] B. Wessel, T. Fritz, T. Busche, P. Rizzoli, G. Krieger, and M. Zink, *TanDEM-X Ground Segment DEM Product Specification Document*, TD-GS-PS-0021, Issue 3.1, DLR, 2016.

[11] T. Fritz, B. Brautigam, G. Krieger, and M. Zink, *TanDEM-X Ground Segment - TanDEM-X Experimental Product Description*, TD-GS-PS-3028, Issue 1.2, 1st ed., DLR, 2012.

[12] S. Duque, U. Balss, C. Rossi, T. Fritz, and W. Balzer, *CoSSC Generation and Interferometric Considerations*, TD-PGS-TN-3129, DLR, 2012.

[13] E. Weber Hoen and H. Zebker, "Penetration depths inferred from interferometric volume decorrelation observed over the Greenland ice sheet," *IEEE Trans. Geosci. Remote Sens.*, vol. 38, no. 6, pp. 2571–2583, Nov. 2000.

[14] E. Rignot, K. Echelmeyer, and W. Krabill, "Penetration depth of interferometric synthetic-aperture radar signals in snow and ice," *Geophys. Res. Lett.*, vol. 28, no. 18, pp. 3501–3504, 2001.

[15] S. Hensley, D. Moller, S. Oveisgharan, T. Michel, and X. Wu, "Ka-band mapping and measurements of interferometric penetration of the Greenland ice sheets by the glistin radar," *IEEE J. Sel. Topics Appl. Earth Observ. Remote Sens.*, vol. 9, no. 6, pp. 2436–2450, Jun. 2016.

[16] G. Fischer, K. P. Papathanassiou, and I. Hajnsek, "Modeling and compensation of the penetration bias in InSAR DEMs of ice sheets at different frequencies," *IEEE J. Sel. Topics Appl. Earth Observ. Remote Sens.*, vol. 13, pp. 2698–2707, May 2020.

[17] S. Leinss, A. Wiesmann, J. Lemmetyinen, and I. Hajnsek, "Snow water equivalent of dry snow measured by differential interferometry," *IEEE J. Sel. Topics Appl. Earth Observ. Remote Sens.*, vol. 8, no. 8, pp. 3773–3790, Aug. 2015.

[18] S. Abdullahi, B. Wessel, M. Huber, A. Wendleder, A. Roth, and C. Kuenzer, "Estimating penetration-related x-band InSAR elevation bias: A study over the Greenland ice sheet," *Remote Sens.*, vol. 11, no. 24, pp. 1–19, Art. no. 2903. 2019, doi: 10.3390/rs11242903.

[19] J. Dall, "InSAR elevation bias caused by penetration into uniform volumes," *IEEE Trans. Geosci. Remote Sens.*, vol. 45, no. 7, pp. 2319–2324, Jul. 2007.

[20] J. Gardelle, E. Berthier, Y. Arnaud, and A. Kääb, "Region-wide glacier mass balances over the Pamir-Karakoram-Himalaya during 1999–2011," *Cryosphere*, vol. 7, no. 4, pp. 1263–1286, 2013.

[21] B. Wessel, A. Bertram, A. Gruber, S. Bemm, and S. Dech, "A new high-resolution elevation model of Greenland derived from TanDEM-X," *ISPRS Ann. Photogramm. Remote Sens. Spatial Inform. Sci.*, vol. 3, pp. 9–16, 2016.

[22] V. Round, S. Leinss, M. Huss, C. Haemmig, and I. Hajnsek, "Surge dynamics and lake outbursts of Kyagar glacier, Karakoram," *Cryosphere*, vol. 11, no. 2, pp. 723–739, 2017.

[23] H. Zebker and J. Villasenor, "Decorrelation in interferometric radar echoes," *IEEE Trans. Geosci. Remote Sens.*, vol. 30, no. 5, pp. 950–959, Sep. 1992.

[24] P. Rizzoli, M. Martone, B. Braeutigam, H. Rott, and A. Moreira, "Deriving Greenland ice sheet properties from TanDEM-X mission data," in *Proc. EUSAR 2016: 11th Eur. Conf. Synthetic Aperture Radar, VDE*, 2016, pp. 1–4.

[25] G. Fischer, K. P. Papathanassiou, and I. Hajnsek, "Modeling multifrequency Pol-InSAR data from the percolation zone of the Greenland ice sheet," *IEEE Trans. Geosci. Remote Sens.*, vol. 57, no. 4, pp. 1963–1976, 2018.

[26] S. Leinss, O. Antropov, J. Vehviläinen, J. Lemmetyinen, I. Hajnsek, and J. Praks, "Wet snow depth from TanDEM-X single-pass InSAR DEM differencing," in *Proc. IEEE Int. Geosci. Remote Sens. Symp.*, 2018, pp. 8500–8503.

[27] M. Martone, B. Bräutigam, P. Rizzoli, N. Yague-Martinez, and G. Krieger, "Enhancing interferometric SAR performance over sandy areas: Experience from the TanDEM-X mission," *IEEE J. Sel. Topics Appl. Earth Observ. Remote Sens.*, vol. 9, no. 3, pp. 1036–1046, Mar. 2016.

[28] J.-S. Lee and E. Pottier, *Polarimetric Radar Imaging*. Boca Raton, FL, USA: CRC Press, 2009.

[29] S. Cloude, *Polarisation - Applications in Remote Sensing*. New York, USA: Oxford University Press, 2010.

[30] S. R. Cloude and K. P. Papathanassiou, "Polarimetric SAR interferometry," *IEEE Trans. Geosci. Remote Sens.*, vol. 36, no. 5, pp. 1551–1565, Sep. 1998.

[31] J. M. Lopez-Sanchez, F. Vicente-Guijalba, E. Erten, M. Campos-Taberner, and F. J. Garcia-Haro, "Retrieval of vegetation height in rice fields using polarimetric SAR interferometry with TanDEM-X data," *Remote Sens. Environ.*, vol. 192, pp. 30–44, 2017.

[32] F. Kugler, D. Schulze, I. Hajnsek, H. Pretzsch, and K. P. Papathanassiou, "TanDEM-X Pol-InSAR performance for forest height estimation," *IEEE Trans. Geosci. Remote Sens.*, vol. 52, no. 10, pp. 6404–6422, Oct. 2014.

[33] S. Leinss, H. Löwe, M. Proksch, J. Lemmetyinen, A. Wiesmann, and I. Hajnsek, "Anisotropy of seasonal snow measured by polarimetric phase differences in radar time series," *Cryosphere*, vol. 10, no. 1, pp. 1–28, 2016.

[34] S. Leinss, G. Parrella, and I. Hajnsek, "Snow height determination by polarimetric phase differences in x-band SAR data," *IEEE J. Sel. Topics Appl. Earth Observ. Remote Sens.*, vol. 7, no. 9, pp. 3794–3810, Sep. 2014.

[35] S. Leinss, H. Löwe, M. Proksch, and A. Kontu, "Modeling the evolution of the structural anisotropy of snow," *Cryosphere*, vol. 14, no. 1, pp. 51–75, 2020.

[36] T. Strozzi, A. Luckman, T. Murray, U. Wegmüller, and C. L. Werner, "Glacier motion estimation using SAR offset-tracking procedures," *IEEE Trans. Geosci. Remote Sens.*, vol. 40, no. 11, pp. 2384–2391, Nov. 2002.

[37] G. Jouvet, M. Huss, M. Funk, and H. Blatter, "Modelling the retreat of grosser Aletschgletscher, Switzerland, in a changing climate," *J. Glaciol.*, vol. 57, no. 206, pp. 1033–1045, 2011.

[38] G. Jouvet and M. Huss, "Future retreat of great Aletsch glacier," *J. Glaciol.*, vol. 65, no. 253, pp. 869–872, 2019.

[39] B. Sevruk and K. Mieglitz, "The effect of topography, season and weather situation on daily precipitation gradients in 60 swiss valleys," *Water Sci. Technol.*, vol. 45, no. 2, pp. 41–48, 2002.

[40] S. Kotlarski, T. Bosshard, D. Lüthi, P. Pall, and C. Schär, "Elevation gradients of European climate change in the regional climate model COSMO-CLM," *Climatic Change*, vol. 112, no. 2, pp. 189–215, 2011.

[41] C. W. Chen and H. A. Zebker, "*Snaphu: Statistical-Cost, Network-Flow Algorithm for Phase Unwrapping (ver. 1.4.2)*," 2003. [Online]. Available: http://nova.stanford.edu/sar_group/snaphu/

[42] P. Rosen *et al.*, "Synthetic aperture radar interferometry," *Proc. IEEE*, vol. 88, no. 3, pp. 333–382, Mar. 2000.

[43] A. Ferretti, A. Monti-Guarnieri, C. Prati, and F. Rocca, *InSAR Principles: Guidelines for SAR Interferometry Processing and Interpretation*, in K. Fletcher, Ed. Auckland, New Zealand: ESA Publications, 2007.
[44] G. H. Fisher and B. T. Welsch, "FLCT: A fast, efficient method for performing local correlation tracking," *Subsurface Atmos. Influences Sol. Activity*, vol. 383, 2008, Art. no. 373.
[45] B. Zitová and J. Flusser, "Image registration methods: A survey," *Image Vis. Comput.*, vol. 21, pp. 977–1000, 2003.
[46] S. K. Park and R. A. Schowengerdt, "Image reconstruction by parametric cubic convolution," *Computer Vis., Graph., Image Process.*, vol. 23, no. 3, pp. 258–272, 1983.
[47] R. Hanssen and R. Bamler, "Evaluation of interpolation kernels for SAR interferometry," *IEEE Trans. Geosci. Remote Sens.*, vol. 37, no. 1, pp. 318–321, Jan. 1999.
[48] O. Frey, E. Meier, D. Nüesch, and A. Roth, "Geometric error budget analysis for TerraSAR-X," in *Proc. 5th Eur. Conf. Synthetic Aperture Radar EUSAR*, 2004, pp. 513–516.
[49] Swisstopo, "Reframe," Accessed: Nov. 9, 2020. [Online]. Available: https://www.swisstopo.admin.ch/en/maps-data-online/calculation-services/reframe.html
[50] G. Krieger *et al.*, "TanDEM-X: A satellite formation for high-resolution SAR interferometry," *IEEE Trans. Geosci. Remote Sens.*, vol. 45, no. 11, pp. 3317–3341, Nov. 2007.
[51] S. Leinss, "Depth, anisotropy, and water equivalent of snow estimated by radar interferometry and polarimetry," Ph.D. dissertation, ETH Zürich, Zürich, Switzerland, 2015.
[52] M. Schwabisch, "A fast and efficient technique for SAR interferogram geocoding," in *Proc. IEEE Int. Geosci. Remote Sens. Symp.*, vol. 2, 1998, pp. 1100–1102.
[53] R. Bamler and P. Hartl, "Synthetic aperture radar interferometry," *Inverse Prob.*, vol. 14, pp. R1–R54, 1998.
[54] R. F. Hanssen, *Radar Interferometry: Data Interpretation and Error Analysis*. Dordrecht, Netherlands: Springer, 2001.
[55] F. Gatelli, A. Guamieri, F. Parizzi, P. Pasquali, C. Prati, and F. Rocca, "The wavenumber shift in SAR interferometry," *IEEE Trans. Geosci. Remote Sens.*, vol. 32, no. 4, pp. 855–865, Jul. 1994.
[56] R. Bamler and G. W. Davidson, "Multiresolution signal representation for phase unwrapping and interferometric SAR processing," in *Proc. IEEE Int. Geosci. Remote Sens. Symp.*, vol. 2, 1997, pp. 865–868.
[57] A. Reigber, "Range dependent spectral filtering to minimize the baseline decorrelation in airborne SAR interferometry," in *Proc. IEEE Int. Geosci. Remote Sens. Symp.*, vol. 3, 1999, pp. 1721–1723.
[58] M. Santoro, C. Werner, U. Wegmüller, and O. Cartus, "Improvement of interferometric SAR coherence estimates by slope-adaptive range common-band filtering." in *Proc. IEEE Int. Geosci. Remote Sens. Symp., IEEE*, 2007, pp. 129–132.
[59] W. H. Press, S. Teukolsky, W. T. Vetterling, and B. P. Flannery, *Numerical Recipes: The Art of Scientific Computing*, 2nd ed. Cambridge, U.K.: Cambridge University Press, 1992.
[60] M. Huss, A. Bauder, M. Funk, and R. Hock, "Determination of the seasonal mass balance of four alpine glaciers since 1865," *J. Geophys. Research: Earth Surf.*, vol. 113, no. F1, pp. 1–11, 2008.
[61] S. Suter, M. Laternser, W. Haeberli, R. Frauenfelder, and M. Hoelzle, "Cold firn and ice of high-altitude glaciers in the alps: Measurements and distribution modelling," *J. Glaciol.*, vol. 47, no. 156, pp. 85–96, 2001.
[62] Meteoschweiz, "Klima bulletin November 2011," Bundesamt für Meteorologie und Klimatologie MeteoSchweiz, Tech. Rep., 2012.
[63] M. Begert and C. Frei, "Long-term area-mean temperature series for switzerland-combining homogenized station data and high resolution grid data," *Int. J. Climatol.*, vol. 38, no. 6, pp. 2792–2807, 2018.
[64] M. Begert and C. Frei, Area-Mean Temperatures of Northern Switzerland $>$ 1000 m a.s.l. 1864-2020. CAT-Version: 1.3.5. 2020. [Online]. Available: https://www.meteoschweiz.admin.ch/home/klima/schweizer-klima-im-detail/schweizer-temperaturmittel/daten-schweizer-temperaturmittel.html

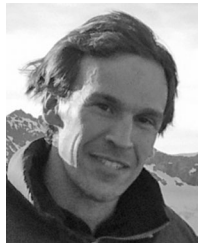

Silvan Leinss (Senior Member, IEEE) received the Diploma degree in laser physics from the University of Constance, Konstanz, Germany, in 2008, and the Ph.D. degree in radar remote sensing from ETH Zürich, Zürich, Switzerland, in 2016.

He was working in the field of coherent light scattering at the University of Constance in 2009 and in the field of light scattering statistics at Bose-Einstein-Condensates, ETH Zurich in 2010. Since 2021, he has been with the Laboratoire d'Informatique, Systémes, Traitement de l'Information et de la Connaissance (LISTIC), Polytech Annecy-Chambéry, Université de Savoie Mont Blanc. He specialized in applications of synthetic aperture remote sensing to observe dynamics of the cryosphere. His research interests include electromagnetic scattering properties of ice and snow, radar interferometry and polarimetry, generation of digital elevation models, glacier offset tracking, modeling of snow dynamics, and analysis of natural hazards.

Dr. Leinss is the recipient of the Helmut-Rott-Prize for his excellent contributions for remote sensing of the cryosphere.

Philipp Bernhard (Student Member, IEEE) received the M.Sc. degree in physics in 2016 from ETH Zürich, Zürich, Switzerland, where he is currently working toward the Ph.D. degree in remote sensing.

He worked on Galaxy Simulations and the evolution of Super Massive Black Holes at ETH Zürich. His main research interests are on permafrost thaw in the arctic with a special emphasis on retrogressive thaw slumps. For this, he works on the generation of microwave digital elevation models, SAR data processing, and on the fusion of different remote sensing products for large-scale applications.